Magnetization dynamics in racetrack memory

Please check the document version of this publication:

• A submitted manuscript is the version of the article upon submission and before peer-review. There can be important differences between the submitted version and the official published version of record. People interested in the research are advised to contact the author for the final version of the publication, or visit the DOI to the publisher's website.
• The final author version and the galley proof are versions of the publication after peer review.
• The final published version features the final layout of the paper including the volume, issue and page numbers.

Link to publication

Magnetization Dynamics in Racetrack Memory

PROEFSCHRIFT

ter verkrijging van de graad van doctor aan de
Technische Universiteit Eindhoven, op gezag van de
rector magnificus, prof.dr.ir. C.J. van Duijn, voor een
commissie aangewezen door het College voor
Promoties in het openbaar te verdedigen
op vrijdag 26 juni 2009 om 16.00 uur

door

Bastiaan Bergman

geboren te Schiedam

Dit proefschrift is goedgekeurd door de promotoren:

prof.dr. B. Koopmans

en

prof.dr.sc.nat.h.c.mult. S.S.P. Parkin F.R.S. N.A.S. N.A.E.

CONTENTS

C h a p t e r   O n e

Introduction

This chapter will introduce the scope of this thesis. After a short introduction to the field of Spintronics I will introduce the main subject of study: the Racetrack memory; a memory type with beneficial properties that potentially lead to a universal memory that is non-volatile, fast and cost effective. Research in this thesis is aimed at enabling Racetrack. Subsequent paragraphs in this chapter will further introduce the detailed aspects of Racetrack and form a fundamental basis. Finally in the last paragraphs I will give a short summary of the current state of research on this subject and determine the scope of this thesis.

Present information technology is based on electron transport and magnetism. Magnetism has been most successful in high-density storage, such as hard disks. For the integration of magnetic storage into electronic circuits, mechanisms are necessary to convert electric current into magnetic information and vice versa. The most common and oldest electro-magnetic coupling is the one arising from Faraday's law, discovered in the early nineteenth century (Figure 1.1). Faraday's law describes the *electro motive force* induced by a magnetic field in a wire loop. This electro motive force, which in fact is an electrical current can be used to read information that is stored in magnetic bits. The opposite was first discovered by Oersted: an electrical current through a wire loop generates a magnetic field. This field can be applied to write information in magnetic bits.

Both mechanisms have been replaced by various s*pintronic* [1] effects; effects based on the spin quantum property of an electron and subsequent coupling to the charge property of an electron. A mechanism called Anisotropic Magneto Resistance (AMR) [2] is more efficient than using Faraday induction and is used in magnetic tape and hard disks since the early days. In the late twentieth century AMR has been replaced by Giant Magneto Resistance (GMR) [3, 4] followed quickly by Tunneling Magneto Resistance (TMR) [5] for reading magnetic bits in most commercial magnetic recording systems. Writing of magnetic bits in today's commercial recording systems, on the other hand, still relies on the Oersted field generated by a wire loop. A spintronic alternative that potentially could take its place as a writing mechanism is Spin Transfer Torque (STT)[i]. STT refers to the ability of conduction electrons to transport the local magnetization of the host material over prolonged distances and is discussed in detail in chapter 1.3.4. Recent achievements in STT systems has enabled Magnetic Random Access Memory (MRAM) [6, 7] which now nears the point of commercialization[ii]. STT-MRAM combines the best properties of two kinds, first it is, as a magnetic system, nonvolatile and secondly, as a chip memory, it is fast and not susceptible to wear.

Yet another step of further integration of magnetic memory and electronic accessibility is the *Racetrack* memory as envisioned by Stuart Parkin. In Racetrack memory the STT

---

[i] Also referred to in the literature and in this thesis as Spin Momentum Transfer (SMT)

[ii] IBM and TDK have produced a 4-Kbit test device in a joint effort; Everspin, Grandis, Crocus Technologies and Hynix & Samsung have all announced to produce demonstration STT-MRAM chips by the end of 2009.

effect is not only used to change the magnetization of predefined magnetic bits, it is also used to push several magnetic domains of uniform magnetization through a long magnetic nanowire. Trains of binary information encoded in magnetic domains are so transported to the location in the wire where they are stored for a prolonged period of time. Racetrack potentially combines the nonvolatility of magnetic storage, high speed and low wear of solid state memory and the price per bit of mass storage devices such as hard disc drives (HDD's). Details of the conceptual Racetrack memory and the challenges for further development are discussed in chapter 1.1.
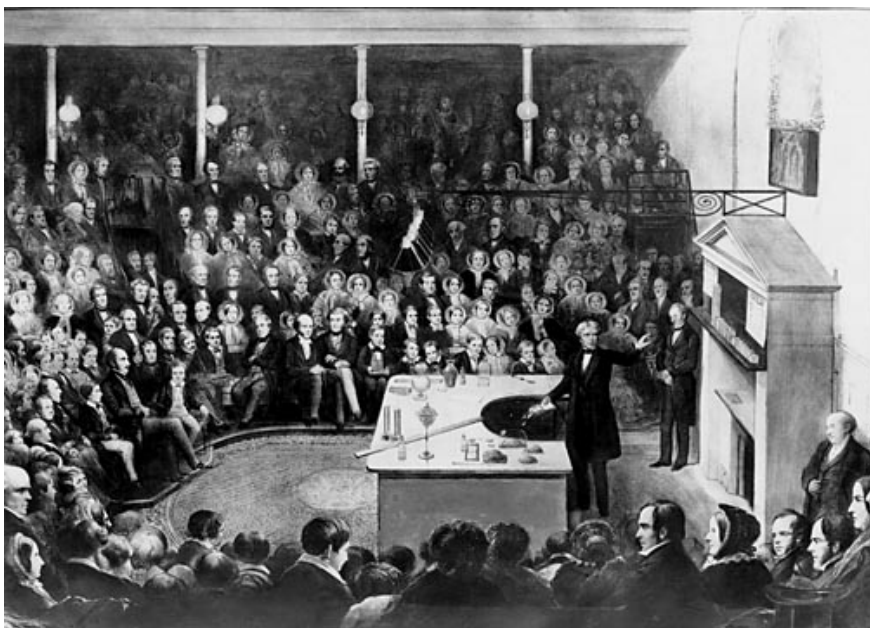
Figure 1.1 27th December 1855, inventor and scientist Michael Faraday lectures at the Royal Institution the Christmas lecture for children which were crowded with interested listeners. The Prince Consort with his sons, the Prince of Wales and the Duke of Edinburgh are seated in the front row facing Faraday. From a painting by Alexander Blaikley.

The work presented in this dissertation is aimed at further enabling the Racetrack memory. The concept of the Racetrack memory itself will be introduced in the next paragraph. Bits of information are stored in Racetrack as magnetic domain walls (DWs). These DWs can be pushed around by current pulses in order to transport them from the read/write device to the place where they are stored. Of key importance to Racetrack is the ability to control dynamic domains in a highly predictable way, hence good understanding of magnetization dynamics is needed. Chapter 1.3 introduces successively the intrinsic precessional motion of local magnetic moments exposed to an

external magnetic field; the phenomenological description of damping of magnetization motion; a 1-dimensional (1D) analytical model describing magnetization motion in nano-sized Racetrack wires and finally the Spin transfer torque effect, the mechanism of key importance where Racetrack relies upon.

1.1 Magnetic Racetrack Memory

Racetrack memory as envisioned by Stuart Parkin [8-13] is a chip based magnetic memory where bits of information are stored as magnetic domains in nano-sized magnetic wires. Little magnetic domains are injected at the bottom of a U shaped wire and transported up into one of the wire ends by a current through the wire using the phenomenon of STT. By writing successive bits and pushing them up in the nanowire with nanosecond long current pulses data can be written in the wire. Reading occurs by pushing the domains back with reversed current pulses towards a reading device such as a TMR sensor at the chip surface. To prevent data loss during readout, wires are U shaped; successive domains are then shifted from one end of the wire through the bottom part of the U to the other end of the wire. Figure 1.2 (a) shows such a U shaped wire with the reading and writing device at the bottom of the U on the chip surface. Bit positions along the nanowire are defined by pining sites. Pinning sites can be fabricated by for example varying the cross-section of the wire or by modulating the magnetic material. Besides controlling the bit length, this also aids the stability of the bits against external perturbations such as thermal fluctuations and stray fields from neighboring wires. Writing of a bit is done by switching the magnetization direction of a domain by means of a localized external field obtained from for example the Oersted field from a crossing wire. Alternatively writing could be performed by means of STT with passing a current from a magnetic nano-element into the wire or by using the fringing fields of a DW in a proximal nanowire writing element.

To shift the DWs along the nanowire the use of nanosecond long current pulses and subsequently the mechanism of STT is elemental. Application of a uniform field would move opposite DWs in opposite directions leading eventually to the annihilation of DWs and thus to loss of data. The nano wires need to be sufficiently small in diameter (< 500 nm) for the STT effect to dominate over the self-field of the current. By making the nanowires sufficiently tall, 10 to 100 domains can be stored per nanowire.
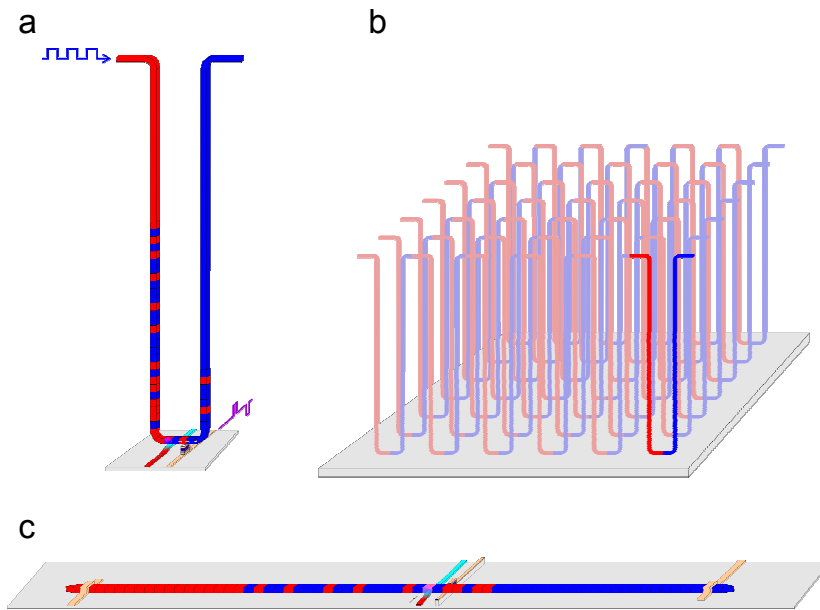
Figure 1.2 (a) Racetrack memory is a ferromagnetic nano-sized wire, with data encoded as a pattern of magnetic domains (bright and dark). Nanosecond long current pulses shift the entire pattern of DWs coherently along the nanowire past reading and writing elements. (b) High data density is obtained by fabricating an array of such wires on the chip surface. (c) A horizontal configuration could initially be fabricated. Even in this configuration, which is easier to fabricate, data densities can be obtained that could potentially compete with nearly all solid state memory types.

By fabricating the nanowires perpendicular on the chip surface the chip area occupied by each wire area is kept to a minimum and very high data densities can potentially be obtained. However, fabricating such wires is a substantial challenge and a much simpler 2-dimensional geometry (Figure 1.2 (c)) would already be competitive to most solid state memory types. Moreover such planar geometry is also beneficial for exploring the physics of domain motion in Racetrack nanowires in a laboratory environment. In chapter 2.2 a chip made at IBM to test horizontal Racetrack memory magnetic wires is introduced. This test structure is then used for all the experiments shown in this thesis.

Because there are no moving parts involved and Racetrack is a purely solid-state memory it has the potential to be a fast random access memory that can compete with most solid state memory types. Secondly Racetrack stores bits of data as magnetic domains and thus retains its contents even when unpowered. This is a great advantage

over traditional RAM memory as no 'boot up' is required. Thirdly, the 3-dimensional Racetrack could potentially obtain such high data densities that the price per bit can become comparable to or even lower than that of HDD's. Finally, when Racetrack is comparable or better than both the internal RAM memory and the external storage HDD of computer systems it can replace both thereby significantly simplifying the overall system architecture [8].

The key concept and one of the most challenging aspects of Racetrack is the controlled movement of DWs along the nanowire by means of current pulses. Current driven DW motion has been studied in a number of materials and geometries. We here focus on permalloy ($Ni_{81}Fe_{19}$) Racetrack nano wires with square cross-section ranging in thickness form 10 to 20 nm and width from 100 to 500 nm. Most studies on current induced DW motion report of a critical current below which no DW motion is observed. Critical currents in permalloy range from 10^9 to 10^{12} A/m^2 depending on the measurement technique and geometry [14]. At such high current densities significant joule heating of the nanowire occurs and temperatures close to the Curie temperature may be obtained. This is of major concern first because reaching the Curie temperature would erase all data but also getting close to the Curie temperature could already cause instabilities by, for example, the creation or annihilation of DWs. Secondly the temperatures obtained may be so high that structural damage occurs to the nanowire.

Beside material and geometry dependence other approaches to lower the critical current have successfully been investigated. Thomas et al. [15] showed the possibility to de-pin a DW from a notch by applying a series of current pulses matching to the oscillatory resonance frequency of the DW. In doing so they were able to resonantly amplify the DW motion which eventually de-pins the DW. Thus by applying a well timed series of smaller current pulses one can de-lodge and move DWs where supplying the same current density in DC would not affect the DW. That control is a subtle and important issue as well, is demonstrated by a similar experiment. By again using current pulses timed in accordance with the resonance frequency of the DW it is possible to de-lodge and propagate a DW in the direction opposite to the electron flow [16].

In the next paragraphs details of the static structure of DWs will be addressed. Then, in chapter 1.3, the dynamics of DWs in motion in Racetrack nanowires will be further explained.

1.2 Magnetic Domains

Weiss first postulated the concept of magnetic domains [17] to explain the extremely high permeability of ferromagnetic materials which could be done by assuming that the sample was divided into multiple fully magnetized regions. The concept was further exploited by Barkhausen [18] and finally confirmed in the 1930s with the work of Bitter [19].
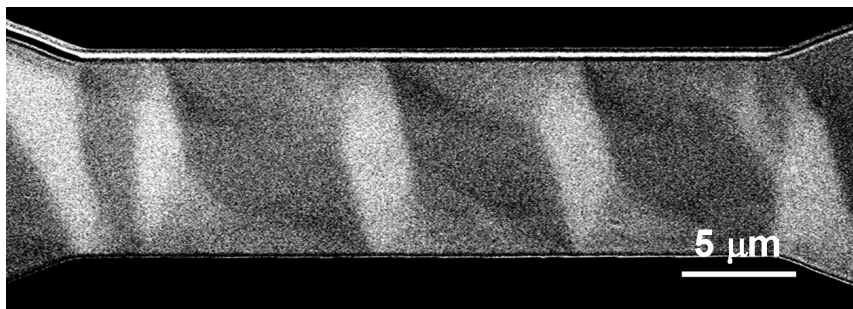
Figure 1.3 Wide field of view Kerr microscope image of a Co meso-structure of 10 micron wide. Different shades of gray are obtained for areas with different magnetization direction. Visible are the closure domains that reduce the total magneto-static energy by reducing the wringing field lines.

Magnetic domains are formed by the competition between the various energy terms involved in a magnetic object. The energy of a magnetic structure is the sum of the exchange energy, the anisotropy energy, the Zeeman energy and the demagnetization energy. The magnetic system seeks to minimize its overall free energy. Since the magnitude of the magnetization cannot change the way to minimize the energy is to vary the direction of the magnetization. The exchange energy seeks to align the spins with each other, the anisotropy energy seeks to align the spins with an axis determined by the crystal structure, the Zeeman energy aligns the spins with an external field. Minimization of these energies will lead to some compromise that leads to the lowest overall energy direction for the magnetization. When also the magneto static dipole-dipole interaction is taken into account, known as the demagnetization energy, a non-uniform magnetization will generally be found as the lowest compromise of the overall energy. Short range exchange energy will prevail a configuration with the spins aligned, large range dipole-dipole interaction will however prevail a magnetic state with minimal net magnetization. Typically this competition leads to large domains with uniform magnetization separated by narrow intermediate regions, called the domain walls.

Figure 1.3 shows an optical Kerr image of a typical domain formation in a permalloy thin film structure.
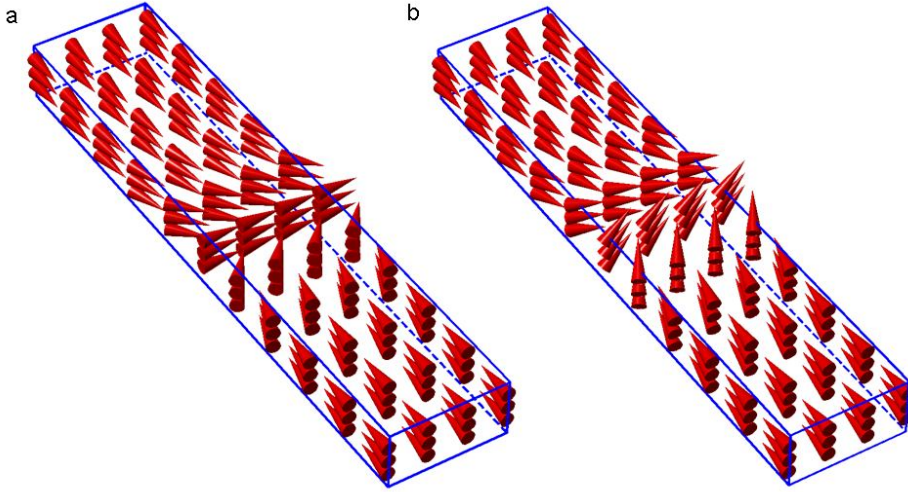
Figure 1.4 Neél domain walls in nano-strips. (a) no DW canting out of the plane ($\psi = 0$), (b) DW is partially canted out of the plane ($\psi = \pi/4$).

In magnetic nanowires where the thickness and width is so small that the magnetization can be assumed uniform over the thickness and width, relative simple calculation of the DW structure is possible. Due to the large demagnetization field induced by the thin film, rotation of the magnetization in a static domain wall within the plane of the thin film is favored, as depicted in Figure 1.4 (a). Only in the dynamic case, as discussed in the next chapter, chapter 1.3.3, a finite angle, ψ, out of the plane may exist which is depicted in Figure 1.4 (b). By calculating the minimum of the total energy involving all energy components including the dipole-dipole interaction one can determine the wall profile which has been calculated [20] for the Neél wall as shown in Figure 1.4 (a) and is given by:

$$\theta(x) = 2\arctan\left(\exp\left(\frac{x - x_0}{\Delta}\right)\right), \tag{1.1}$$

with θ the angle of the local magnetization in the wall, x the position along the nanowire, x_0 the central position of the domain wall and Δ the width of the domain wall. For real physical systems of interest here, which may have non uniform magnetization in any direction analytical calculation becomes too complicated. Numerical micro-magnetic calculations are then the avenue of choice. Figure 1.5 shows the calculated results for two permalloy nanowires of 20×100 nm and 20×300 nm cross section respectively.

The smaller nanowire still shows good agreement with the above shown Neél wall, called transverse DW in this context. In the larger nanowire another DW structure becomes favorable where the true 3 dimensional size of the structure is used to further lower the total overall DW energy. This so called vortex DW is energetically favorable in nanowires with a width of 200 nm or more when the thickness is 20 nm [21, 22].
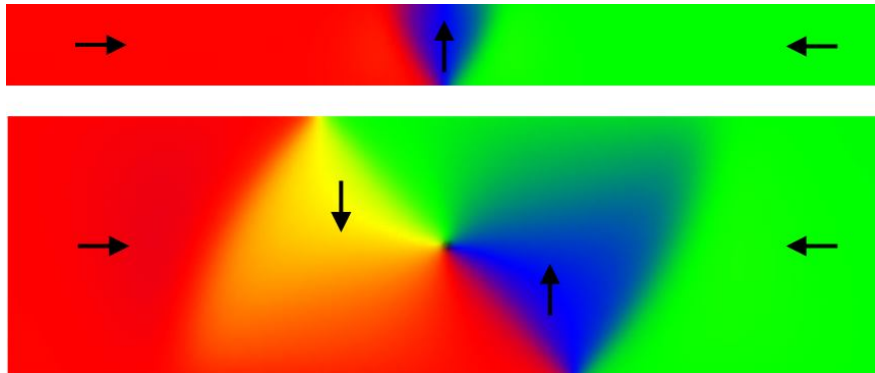
Figure 1.5 Micro magnetic simulation of the stable state of a DW in a 20 nm thick permalloy nanowire of 100 nm (top) and 300 nm (bottom) width.

1.3 Magnetization Dynamics

In this paragraph we will derive equations of motion for a DW in a nano-sized wire. First the dynamics of localized magnetic moments will be illuminated, then we will transform the obtained equations into an Euler Lagrange form. Finally by assuming the possible macroscopic magnetization structure the Euler equations of motion will be put into coordinates of a rigid DW. The so obtained analytical equations are shown to be very useful for assessing macroscopic properties of a propagating DW.

1.3.1 Precession

Equivalent to a current carrying wire loop an electron spinning about its axis induces a magnetic field [23]. The magnitude of such magnetic field, $\mathbf{M}$, is related to the angular momentum associated with electron spin, $\mathbf{S}$, by the gyromagnetic ratio γ:

$$\mathbf{M} = \gamma \mathbf{S}.$$
(1.2)

As first demonstrated by Faraday, a magnetic field exerts a torque, $\mathbf{T}$, on a current carrying loop given by:

$$\mathbf{T} = \mathbf{M} \times \mathbf{H} . \tag{1.3}$$

Classically, torque exerted on a rigid body induces an angular momentum, $\mathbf{L}$, given by:

$$\frac{d\mathbf{L}}{dt} = \mathbf{T} . \tag{1.4}$$

Quantum mechanically equation (1.4) remains valid when $\mathbf{L}$ and $\mathbf{T}$ are interpreted as operators in a Hilbert space and can be used for a spin system by replacing $\mathbf{L}$ by the operator $\mathbf{S}$:

$$\frac{d\mathbf{S}}{dt} = \mathbf{T} . \tag{1.5}$$

By combining the equations (1.2), (1.3) and (1.5) an equation of motion for the magnetic moment of an electron is obtained:

$$\frac{d\mathbf{M}}{dt} = \gamma \mathbf{M} \times \mathbf{H} . \tag{1.6}$$

Multiplying equation (1.6) with $\mathbf{M}$ shows that the magnitude $|\mathbf{M}|$ does not change, regardless the field, $\mathbf{H}$, applied:

$$\mathbf{M} \cdot \dot{\mathbf{M}} = \frac{d}{dt}|\mathbf{M}|^2 = \mathbf{M} \cdot (\mathbf{M} \times \mathbf{H}) = 0 \tag{1.7}$$

and multiplying the same equation with $\mathbf{H}$ shows that the angle between $\mathbf{H}$ and $\mathbf{M}$ remains constant at all times:

$$\mathbf{H} \cdot \dot{\mathbf{M}} = \frac{d}{dt}[\mathbf{H} \cdot \mathbf{M}] = \mathbf{H} \cdot (\mathbf{M} \times \mathbf{H}) = 0 , \tag{1.8}$$

thus, what equation (1.6) describes is a precessional motion as sketched in Figure 1.6.
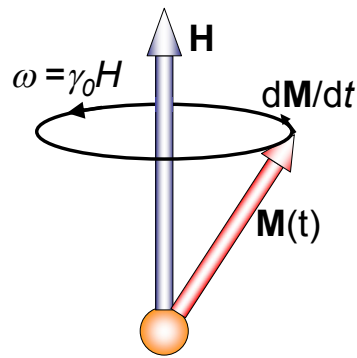
Figure 1.6 Magnetization precession.

Since the magnitude of magnetization remains unchanged it has advantages to rewrite the equation into spherical coordinates. For that we first rewrite the field **H** in terms of potential energy $U(\mathbf{M})$, where $U(\mathbf{M})$ is defined as the work done when **M** rotates against the forces acting on it

$$\mathbf{H} = -\frac{1}{\mu_0} \frac{\partial U(\mathbf{M})}{\partial \mathbf{M}} . \tag{1.9}$$

The potential energy caused by the application of an external field $\mathbf{H}_A$ on a magnetic moment is than given by

$$U = -\mu_0 \left(\mathbf{M} \cdot \mathbf{H}_A \right) \tag{1.10}$$

and is called the Zeeman energy. The precession equation for magnetic moment in spherical coordinates θ and ϕ, as defined in Figure 1.7, is than given by two differential equations:

$$\begin{aligned} \dot{\varphi} &= \frac{\gamma_0}{\mu_0 M_S \sin(\theta)} \frac{\partial U}{\partial \theta} \\ \dot{\theta} &= -\frac{\gamma_0}{\mu_0 M_S \sin(\theta)} \frac{\partial U}{\partial \varphi} \end{aligned} \tag{1.11}$$

These equations could be derived form a Lagrange function [24] as first pointed out by Döring when a Lagrangian, $\mathcal{L}$ is defined as:

$$\mathcal{L} = -\frac{\mu_0 M_S}{\gamma_0} \dot{\varphi} \cos(\theta) - U . \tag{1.12}$$

Magnetization then obeys the classical Euler equations of motion

$$\frac{d}{dt}\left[\frac{\delta \mathcal{L}}{\delta \dot{q}_i}\right] - \frac{\delta \mathcal{L}}{\delta q_i} = 0, \tag{1.13}$$

with $q_i = \theta$ or φ. This describes the precessional motion of a magnetic moment in any potential field U assuming no energy is lost.
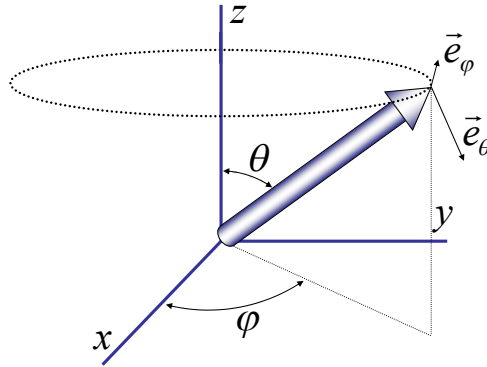
Figure 1.7 Definition of the spherical coordinates used, $\theta \in \{0..\pi\}$ and $\varphi \in \{0..2\pi\}$.

1.3.2 Damping

In real systems, however, energy is dissipated through various avenues and the magnetization motion is *damped* until an equilibrium is reached. Energy dissipation takes place, for example, through the excitation of spin-waves, by the formation of Eddy currents or by direct coupling to other fields, e.g. strain fields. All energy eventually ends up as microscopic thermal motion in the lattice system (phonons), the magnetic system (magnons) or as thermal excitations of conduction electrons. An elegant way to introduce damping in the equations of motion (Eq. (1.13)) is by adding a Rayleigh dissipation function, as proposed by Gilbert[25, 26] and presented in conjunction with experimental data on the first conference on Magnetics and Magnetic Materials in 1956 in Pittsburgh, Pa [27]. In classical mechanics the frictional force is proportional to the velocity of the particle. Frictional forces of this type may be derived in terms of a function $\mathcal{R}$, known as the Rayleigh dissipation function, and is defined as

$$\mathcal{R} = \frac{1}{2}\sum_i \left(k_x v_{i,x}^2 + k_y v_{i,y}^2 + k_z v_{i,z}^2\right), \tag{1.14}$$

where the summation is over the particles of the system [28]. The Euler equations now become

$$\frac{d}{dt}\left[\frac{\delta\mathcal{L}}{\delta\dot{q}_i}\right] - \frac{\delta\mathcal{L}}{\delta q_i} + \frac{\delta\mathcal{R}}{\delta\dot{q}_i} = 0 . \tag{1.15}$$

For a magnetic system the time derivative of magnetization is taken as the equivalent of particle velocity and a Rayleigh function is then defined as [24]

$$\mathcal{R} = \frac{\alpha\mu_0 M_S}{2\gamma_0}\left(\dot{\theta}^2 + \dot{\varphi}^2 \sin^2\theta\right), \tag{1.16}$$

with the Euler equations as defined in(1.15). At this point Gilbert derived the Cartesian differential equation for magnetization dynamics in his original thesis [26] known as the Landau Liftshitz Gilbert (LLG) equation, also in recognition of Landau and Liftshitz who already had arrived at an equation for magnetization dynamics with damping incorporated in a slightly different form. The LGG equation than reads

$$\dot{\mathbf{M}} = -\gamma_0 \mathbf{M}\times\mathbf{H}_{eff} + \frac{\alpha}{M_S}\mathbf{M}\times\dot{\mathbf{M}} . \tag{1.17}$$

The magnetization vector that precesses around the applied field, as depicted in Figure 1.6, will now gradually lose its energy and spiral down to the direction of the applied field. Equation (1.17) can easily be transformed in a more tractable form by eliminating the time derivative of the magnetization[i] in the right hand part of it:

$$(1+\alpha^2)\dot{\mathbf{M}} = -\gamma_0 \mathbf{M}\times\mathbf{H}_{eff} + \frac{\alpha\gamma_0}{M_S}\mathbf{M}\times\left(\mathbf{M}\times\mathbf{H}_{eff}\right) . \tag{1.18}$$

Equation (1.18) is sometimes called the Landau Liftshitz form (LLE) of LLG, even though the original equations from Landau and Liftshitz had a different form of damping incorporated and were not equivalent to the LLG equation [29]. In the next paragraph we will continue with the Lagrange form of the equations and use it to obtain equations of motion in a transformed coordinate system which leads to the very valuable one dimensional equations of motion for domain walls. As developed by Malozemoff and Slonczewski [30] and others in the 1970's.

---

[i] Which can be verified by substituting $\mathbf{M}\times\mathbf{H}$ in the second term on the right hand of (1.18) and use of the vector equality $\mathbf{a}\times(\mathbf{b}\times\mathbf{c}) = (\mathbf{a}\cdot\mathbf{c})\mathbf{b} - (\mathbf{a}\cdot\mathbf{b})\mathbf{c}$.

1.3.3 One Dimensional Model for Domain Wall Motion

The equation for magnetization dynamics in Euler form, Equation (1.15), is very useful for constructing equations for magnetization dynamics pertained to a given class of structures. It has been showed that the structure of prevalence separating two domains in a flat nanowire can be approximated by a Bloch wall in just one dimension [24] while the magnetization is constant in the other two dimensions ($\mathbf{M}(\mathbf{x},t) = \mathbf{M}(x,t)$). If we restrict the configuration space of domain walls to this class of profiles and the only variation in the Euler equations allowed are that of changing the class parameters we can directly obtain equations of motion for the magnetization structure as a whole described by the profile parameters. The Bloch wall is described by its position *q(t)* and its canting out of the plane *ψ(t)* and is given in spherical coordinates by[i]

$$\theta(x,t) = 2\arctan\left(\exp\left(\frac{z - q(t)}{\Delta}\right)\right),$$
$$\varphi(x,t) = \psi(t), \tag{1.19}$$

where *Δ* is the domain wall width. If we now substitute θ and φ in the Lagrangian and Rayleigh function we obtain these functions in terms of *q(t)* and *ψ(t)*. The Euler equations are obtained by seeking stationary points in the integral of $\mathcal{L}$ by variation of the functions q_i. After substitution of θ and φ we first integrate $\mathcal{L}$ over the whole space (*x,y,z*) to eliminate *z*, we obtain[ii]

$$\mathcal{L} = \frac{2\mu_0 M_S S}{\gamma_0}\dot{\psi}q - W, \tag{1.20}$$

where *S* is the surface area of the nanowire cross section and *W=W(q,ψ)* the potential energy of the system as a whole in terms of *q* and *ψ*. Equivalent for $\mathcal{R}$, we obtain

$$\mathcal{R} = \frac{\alpha\mu_0 M_S S}{\gamma_0}\left(\Delta\dot{\psi}^2 + \frac{\dot{q}^2}{\Delta}\right). \tag{1.21}$$

---

[i] q_i refers to any function to vary in the context of the Euler functional analysis, *q* and *q(t)* refer to the DW position along a one dimensional nanowire.

[ii] Note that the function to be integrated over *x,y* and *z* only depends on *z* and note that integration becomes very simple with the useful property $\partial\theta / \partial x = \sin\theta / \Delta$.

Solving the Euler equations (Equation (1.15)) for q_i is $q(t)$ and $\psi(t)$ respectively results in the equations of motion for the domain wall:

$$\frac{\partial W}{\partial q} = \frac{2\mu_0 M_S S}{\gamma_0}\left(\dot{\psi} - \frac{\alpha}{\Delta}\dot{q}\right),$$
$$\frac{\partial W}{\partial \psi} = \frac{2\mu_0 M_S S}{\gamma_0}\left(\dot{q} + \alpha\Delta\dot{\psi}\right). \tag{1.22}$$

With these equations we can describe DW motion as a rigid particle moving in a potential field W in one dimension. In order to perform particular calculations and derive q and ψ we need an explicit expression for the potential energy W where the DW is exposed to. The potential energy for a DW in a flat and narrow nanowire is the sum of several terms. First there is the Zeeman energy caused by the applied field H, as shown before (Equation (1.10)) but now as an energy of the whole nanowire system and in terms of DW position, the Zeeman energy is given by:

$$W_{Zeeman} = -2\mu_0 M_S HSq(t). \tag{1.23}$$

with H the applied field in the direction of the nanowire. Secondly due to the demagnetization energy the DW has an energy that is dependent on the out of the plane canting of the magnetization given by:

$$W_{Demag} = \sigma_0 + 2\Delta H_K M_S \sin^2(\psi), \tag{1.24}$$

where σ_0 represents the internal energy of the DW and is not dependent on q of ψ. Finally we could introduce geometrical features, for example we could define a notch at $q = q_0$ with a certain harmonic potential energy of depth V:

$$W_{Geometric} = V\left(\frac{q}{q_0}\right)^2. \tag{1.25}$$

If we incorporate the ψ dependent parts of the potential energy into the equations (1.22) and solve them for $\dot{\psi}$ and $\dot{q}$ we obtain:

$$(1+\alpha^2)\dot{\psi} = -\frac{\gamma_0}{2M_S S}\frac{dW}{dq} - \frac{\gamma_0\alpha}{2}H_K\sin(2\psi),$$
$$(1+\alpha^2)\dot{q} = \frac{\gamma_0\alpha\Delta}{2M_S S}\frac{dW}{dq} + \frac{\gamma_0\Delta}{2}H_K\sin(2\psi), \tag{1.26}$$

the equations of motion for a rigid DW in a nanowire [14]. It has been pointed out that these equations resemble Hamilton's equations of motion for two canonical conjugate variables q and $2M_S\psi/\gamma$, that is the position and its conjugate momentum. Following this analogy also a DW mass has been defined by Döring, called the Döring mass [31].

Figure 1.8 shows an example of field driven DW motion in a nanowire as calculated by the 1D model. Clearly for an applied field of 9.5 Oe (and lower as we will see in the next paragraph) the DW translates linearly after an initial period of acceleration. The DW structure obtains an out of the plane canting of 45 degrees which remains constant throughout the motion. Conversely, when a field of 10 Oe is applied (or higher, see next paragraph) the DW motion becomes oscillatory where the DW structure continuously rotates around.

Next we will continue with the analytical equations and deduct some general expressions for the DW velocity in two regimes.

Using these equations simple analytical expressions can be derived for the DW velocity. Particularly at small applied fields the DW velocity is linear with the applied field and given by

$$v = \frac{\Delta\gamma H}{\alpha},$$
(1.27)

At these fields the out of plane canting y of the magnetization is linear with the applied field and stationary during DW motion, up to the point where the magnetization is canted out of the plane completely, $\psi = \pi/2$, and no further increase can be accomplished. This happens when the applied field reaches a limit called the Walker breakdown field H_{WB}. This maximum field for stationary DW motion can be directly obtained from (1.26) by assuming $\dot{\psi} = 0$ and $\psi = \pi/2$ given by:

$$H_{WB} = \frac{1}{2}\alpha H_K.$$
(1.28)
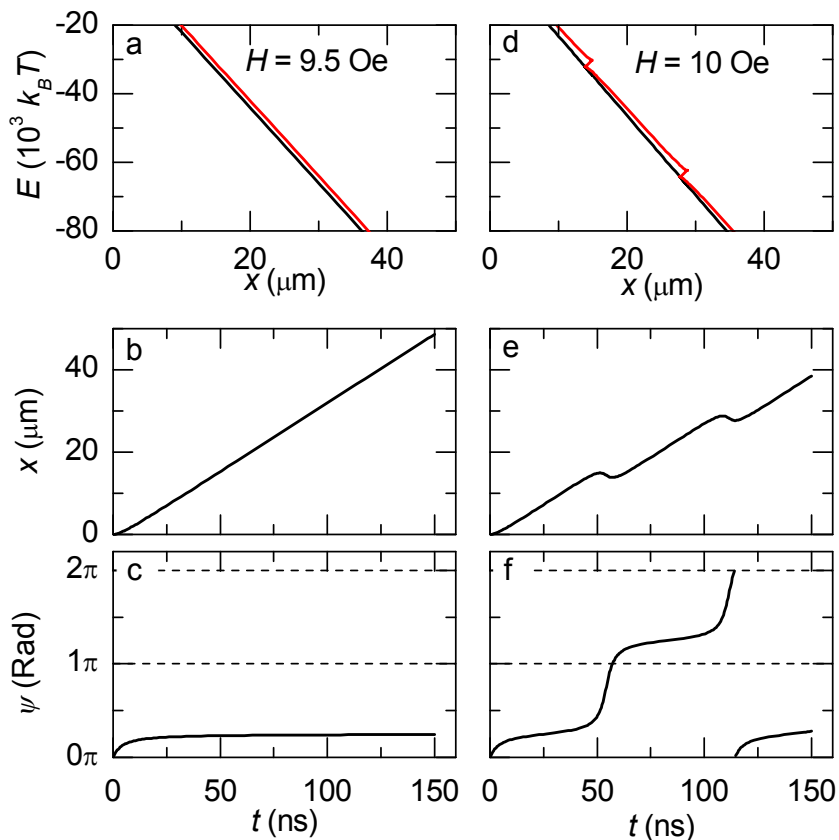
Figure 1.8 one dimensional model calculations of a DW in a nanowire when a driving field is applied of 9.5 Oe (left figures) and 10 Oe (right figures). (a and d) show the potential energy (Zeeman energy) to which the DWs are exposed (black lines) and the DW trajectory (gray lines). (b and e) DW position as function of time. (c and f) Canting angle of the DW structure out of the plane versus time.

When the field is further increased beyond the Walker breakdown field the DW canting becomes unstable and the DW starts to oscillate (see

Figure 1.8 (d,e,f)), this causes the DW velocity to drop. The maximum velocity obtained is thus the velocity at Walker breakdown and given by:

$$v_{max} = \frac{1}{2}\gamma\Delta H_K .$$

(1.29)

Note that when no damping is present, $\alpha = 0$, no DW motion is possible. When $\alpha = 0$, the domain wall tilt ψ will be continuously increasing with time, i.e. the DW rotates continuously. At the same time $\dot{q}$, the DW velocity, will oscillate between $\pm H_K \gamma_0 \Delta / 2$ and no net DW propagation is achieved. This, in first instance counter

intuitive result, can be understood if one realizes that the Zeeman energy contained in the opposite magnetized domain can only be released by dissipation through Gilbert damping. The system lacking such avenue of energy release, never relaxes to the energetically favorable configuration.
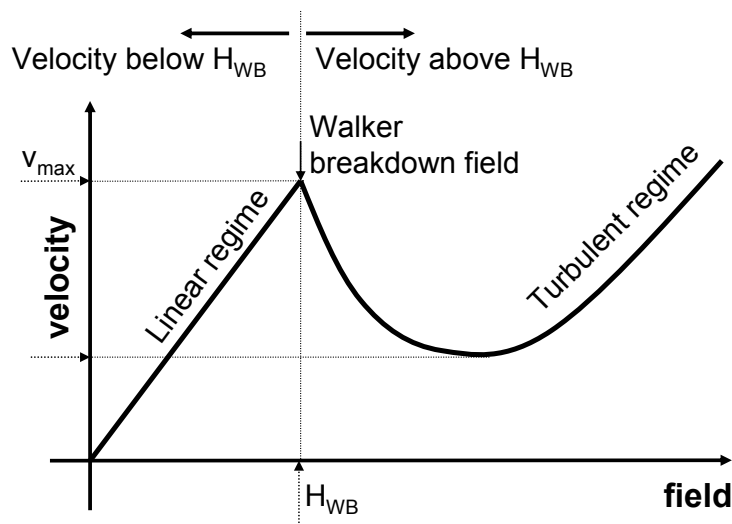
Figure 1.9 DW velocity profile sketch. DW propagation is characterized by two regimes, the linear regime where DW velocity increases linearly with applied field, and the turbulent regime where the DW velocity profile first shows a dip after the Walker breakdown field (H_{WB}) before it further increases.

In Figure 1.9 a sketch of a typical DW velocity profile is shown. In the chapters to come these 1D model expressions will be used to compare the measured DW velocity with effective values for the domain wall width and anisotropy. In chapter 3 the model will be extended to also encompass wire roughness and used to explain measurements of the minimum field needed for DW propagation. In chapter 4 we will continue to extend the 1D model by simulating the Gilbert damping dependence of the minimum propagation field. In chapter 5 we will measure the current induced effects on DW propagation, the theoretical model therefore is introduced in the next paragraph.

1.3.4 Spin Transfer Torque

When a current is passed through a ferromagnetic material, electrons will *polarize*, that is, the spin of the conduction electron will align with the spin of the local electrons carrying the magnetic moment of the material. When the conduction electrons subsequently enter a region of opposite magnetization they will eventually become

polarized again, thereby transferring their spin momentum to the local magnetic moment, as required by the law of conservation of momentum. Therefore, when many electrons are traversing a DW, magnetization from one side of the DW will be transferred to the other side. Effectively the electrons are able to push the DW in the direction of the electron flow[i]. This effect is called the Spin Transfer Torque effect (STT) and was first proposed by Berger [32].

The mechanism is based on s-d exchange interaction between the conduction electrons and the local magnetic moment. This influences the DW dynamics in two different ways. The first contribution is caused by the conduction electrons that experience a torque when traversing a magnetic DW. The consequent change in spin angular momentum is transferred to the localized spins in the domain wall. The second contribution, called exchange torque or non-adiabatic spin transfer, is related to the transfer of spin momentum from the s conduction electrons to the local magnetization. The latter also contributes when a current is traversing two magnetic layers who are separated by a non-magnetic metal layer, as proposed by Slonczewski [33].

The influence of current on DW dynamics is often treated by including two spin torque terms in the LLG equation, equation (1.17). When the current, with current density J, is flowing in one direction, the x-direction the LLG equation including the spin torque terms can be written as

$$\dot{\mathbf{M}} = -\gamma_0 \mathbf{M} \times \mathbf{H}_{eff} + \frac{\alpha}{M_S} \mathbf{M} \times \dot{\mathbf{M}} - \eta J \frac{\partial \mathbf{M}}{\partial x} + \beta \eta J \mathbf{M} \times \frac{\partial \mathbf{M}}{\partial x}, \qquad (1.30)$$

where two last terms are added to the regular LLG equation to describe the effect of current on the magnetization dynamics. The first of these terms expresses the adiabatic spin transfer torque as exerted by a current on magnetic DWs with η the strength of the effect. The second STT term in the equation describes the non-adiabatic current induced effect which relative strength is parameterized by β. The strength of the adiabatic spin torque, η, is widely agreed on [32, 34-36] and given by:

$$\eta = \frac{g\mu_B P}{2eM_S}, \qquad (1.31)$$

---

[i] This is opposite to the direction of the current, since electrical current is defined as the flow of positive charge carriers and electrons are in fact negative charge carriers.

where g is the Land factor, μ_B the Bohr magneton, e the electron charge, M_S the saturation magnetization[i] and P the electron polarization, all of which the values are very well know except for the electron polarization. Estimates for P range from $P = 0.4$ to $P = 0.7$ [37].

The microscopic process of the non-adiabatic term in (1.30) is less well understood. Berger first introduced the non-adiabatic term as a consequence of the Stern-Gerlach force on conduction electrons by the gradient in the s-d exchange field [38]. Others argue this may arise from linear momentum transfer [34] or spin flip scattering [39].

Incorporating the spin torque terms as they appear in equation (1.30) in the 1D model (Equation (1.26)) goes in a similar way as described in chapter 1.3.3 and results in the equations:

$$\begin{aligned}(1+\alpha^2)\dot{\psi} &= -\frac{\gamma_0}{2M_S S}\frac{dW}{dq} - \frac{\gamma_0\alpha}{2}H_K\sin(2\psi) + \frac{(\beta-\alpha)}{\Delta}\eta J, \\ (1+\alpha^2)\dot{q} &= \frac{\gamma_0\alpha\Delta}{2M_S S}\frac{dW}{dq} + \frac{\gamma_0\Delta}{2}H_K\sin(2\psi) + (1+\alpha\beta)\eta J.\end{aligned} \tag{1.32}$$

Equivalently to the procedure in chapter 1.3.3 also expressions for the DW velocity can be deduced. For small applied fields and small currents the DW velocity increases linearly with current and field:

$$v = \frac{\Delta\gamma H}{\alpha} + \frac{\beta\eta}{\alpha}J, \tag{1.33}$$

The maximum field for stationary DW motion is now in general dependent on the applied current and given by:

$$H_{WB} = \frac{1}{2}\alpha H_K - (\beta-\alpha)\frac{\eta}{\gamma\Delta}J. \tag{1.34}$$

When the field is further increased beyond the Walker breakdown field the DW canting becomes unstable and the DW starts to oscillate, this causes the DW velocity to drop. The maximum velocity obtained is thus the velocity at Walker breakdown and given by:

---

[i] With the saturation magnetization M_S we refer, throughout this thesis, to the magnetization at temperature T, not to the magnetization at T = 0 K.

$$v_{\max} = \frac{1}{2}\gamma\Delta H_K + \eta J \ . \qquad (1.35)$$

In chapter 5 we will compare current induced effects on DW propagation with 1D model expectations. Comparison of the Walker breakdown field and DW mobility in a series of samples with increasing Gilbert damping results in numerical values for the spin polarization P as well as for the relative contribution of the non-adiabatic component, β.

1.4 Current State of Research

Mott first introduced the idea of a spin polarized current to explain the kink in the resistivity at the Curie temperature of ferromagnetic materials [40]. Bearing in mind Newton's law, *to every action there is an equal and opposite reaction,* it seems obvious to assume that the spin polarized current could also influence the magnetization of the ferromagnetic material. Berger first predicted [32, 38, 41, 42] and observed [43-45] that a spin polarized current could apply a torque on magnetic domain walls. Early theoretical work by Slonczewski and Berger has put the Spin Transfer Torque (STT) in a framework [33, 46] which has been extended by recent proposals based on a microscopic approach [34, 36, 39, 47, 48]. The topic of current induced DW motion has seen growing interest in recent years due to its promising applications to spintronic devices, such as logic and memory devices. Another factor of importance is the vast improvement of engineering tools for the fabrication of nano-sized structures, which has become available to a broad research community over the last few decades.

1.4.1 Critical Current

Critical current refers to the observed effect that no DW motion exists below a certain minimum current. Many recent studies focused on DW motion in nanowires address the issue of the threshold current density [43, 49-58]. The origin of the critical current has been debated much. Some authors believed the critical current could have an intrinsic origin which would point to pure adiabatic STT ($\beta = 0$) [34-36]. In more recent theoretical work the non-adiabatic term is added, which provides the possibility of current driven DW motion at arbitrarily small current densities [36, 39, 47]. However such a movement at low currents has not been observed in experiments. General belief is that the origin of the critical current must be found in material or geometrical

imperfections of the physical system. Imperfections are also believed to be the cause of a threshold field below which no DW propagation exists and, at the same time, a study from Nakatani et al. [59] has shown that DW propagation velocity could be improved by expressly engineering edge roughness on the nanowire.

1.4.2 Current Induced DW Velocity

An issue of much importance for devices and especially of importance for Racetrack memory is the DW propagation velocity. Current driven DW velocities as high as 110 m/s in permalloy were reported by Hayashi et al. [60] exceeding estimates for the rate at which spin torque could be transferred and suggesting that other mechanisms play a role. Yamanouchi et al. report of DW velocities depending on current density ranging over five orders of magnitude from 10^{-4} m/s to 22 m/s in (Ga,Mn)As [61]. Jubert et al. have shown that DW propagation velocity in permalloy nanowires reduces with the number of current pulses applied. Also they show that the DW velocity depends heavily on the nanowire width [62]. Klaui et al. explain this observation from the DW structure. They observed the DW structure with spin-polarized scanning electron microscopy and recorded a change from vortex to transverse after several subsequent current pulses. Once the DW structure had changed to a transverse DW no further translation happened with further applied current [54].

1.4.3 Control

Another important issue is the controllability of magnetic DWs in nano-sized magnetic structures, of uttermost importance when aimed at building memory or logic devices. Beach et al. [63] have shown experimentally that DW propagation, driven by fields above the Walker breakdown, happens in a precessional fashion. At such high fields, DWs don't move at constant velocity in the direction of the applied field, instead these DWs undergo a continues oscillating change of their internal structure and thereby moving in the opposite direction during part of their oscillatory motion, as it was predicted by Walker. Control of two DWs simultaneously with current was shown quasi statically with magnetic force microscopy imaging between subsequent current pulses [8]. Hayashi et al. showed the controlled motion of three DWs in a permalloy nanowire

by means of electrical current and were able to maintained the DWs intact during several DW-shift cycles [64].

1.5 Scope of this Thesis

After this introduction in chapter 2 of the thesis I will first discuss a magneto optical measurement technique that was developed to measure magnetization dynamics in Racetrack test structures. With deploying a pump-probe scheme, good signal over noise ratio is achieved, enabling the measurement of magnetization dynamics in nanowires much smaller than the focused laser spot. The specific chip design, pulse sequences to optimally control the preparation, propagation and resetting of DWs, as well as the added value of the optical approach are discussed in detail. Experimental results obtained with this measurement technique are then discussed and compared to theoretical models in the chapters 3 to 5.

In chapter 3 I introduce a difference in the minimum field needed to propagate magnetic domains when at rest compared to domains already in motion. Propagation of DWs is proven to be stochastic and propagation probabilities are measured. Measurements show that DWs starting from rest exhibit much more uncertainty in their ability to move upon applied fields than DWs already in motion. An effect that is explained by extending the 1D model to also encompass wire roughness.

In chapter 4 I further develop this extension to the 1D model by investigating nanowire test structures that have different values of the magnetization damping. Stronger damping is obtained by doping of the permalloy nanowires with osmium. The obtained results further establishes the 1D model in general and the wire roughness incorporation specifically. Better understanding of the role of wire roughness could lead to better control of DW dynamics.

Finally in chapter 5 current and field driven magnetic domain wall motion in nano-sized wires is measured, particularly aiming at exploring the efficiency of the non-adiabatic contribution as a function of Gilbert damping. The results in comparison with the 1D model and with micro magnetic simulations lead to a numerical value for the relative contribution of the non-adiabatic spin transfer torque. A pronounced dependence of the measured non-adiabatic spin torque efficiency (βP) on osmium doping concentration was found. This result may be interpreted as a sign that the intensively debated ratio β/α is far from constant over the range of alpha studied.

Measurement Technique

Generation of local magnetic fields at MHz rates for the study of domain wall propagation in magnetic nanowires[i]

We describe a novel technique for generating local magnetic fields at MHz rates along magnetic nanowires. Local and global magnetic fields are generated from buried copper fine-pitch wires fabricated on 200 mm silicon wafers using standard CMOS back-end process technology. In combination with pump-probe scanning Kerr microscopy, we measure the static and dynamic propagation fields of domain walls in permalloy nanowires.

2.1 Introduction

The creation and manipulation of magnetic domain walls (DWs) in magnetic nanowires form the basis of several recently proposed memory and logic devices [8, 64-66]. This has stimulated considerable research into the field and current driven magnetization dynamics of domain walls in nanowire devices [16, 60, 67]. Various techniques have been used to probe the dynamics of domain walls including quasi-static techniques such as magnetic force microscopy [8, 51] and photoemission electron microscopy [68] as well as real time techniques including anisotropic magnetoresistance (AMR) [69], magnetic scanning transmission x-ray microscopy [70, 71], and magneto-optic Kerr effect (MOKE) [72-75].

Among these techniques MOKE is a particularly simple yet powerful means of measuring local magnetization distributions in a wide variety of magnetic materials without perturbing the magnetic structure [76]. To use MOKE to study magnetization dynamics it is typically required that in order to achieve sufficient signal to noise the experiment be repeated many times (perhaps $\sim 10^5$-10^6, depending on the time resolution needed). Since measurements of DW dynamics often require the use of magnetic fields to create and/or manipulate the DWs it would be highly useful to be able to generate local magnetic fields at high repetition rates. Conventional electro-magnets are much too slow due to their large inductance. This can be mitigated by using smaller coils and reduced number of windings but at the expense of lower magnetic fields. In this Letter we demonstrate the fabrication and use of chiplets with two levels of copper fine-pitch wiring which can generate large local (up to ~400 Oe) and global magnetic fields (up to ~50 Oe) at MHz repetition rates.

2.2 CMOS Racetrack Test Structure

The chiplets were fabricated using CMOS wiring interconnect processes on 200 mm diameter silicon wafers[i]. Using a standard damascene process [77] with a 248 nm optical stepper, highly conductive (2-3 $\mu\Omega$ cm), dense (1:1 line and spacing), and small aspect ratio (almost 1:1) copper lines, as narrow as 200 nm wide, are buried in SiO_2 insulator. The copper lines are oriented at 90 degree to the length of the permalloy

---

[i] The chiplets were fabricated in the Microelectronics Research Laboratory, IBM T.J. Watson Research Center.

nanowire so that the fields generated by these lines are oriented along the nanowire. Two levels of copper lines (labeled M1 and M2) are fabricated by the following sequence: (1) chemical vapor deposition of SiO_2, (2) optical lithography and reactive ion etching of the trench, (3) filling the trench with Ta/TaN liner and Cu seed layer and overfilling with electroplated Cu, and (4) chemical mechanical polishing of Cu and liner to complete the trench processing. To obtain an extremely flat surface, an extra thick SiCHN[i] layer is added after the second Cu level (M2) and is smoothed by a CMP planarization process. The root mean square surface roughness of the final device was measured to be a few Angstrom. A very smooth surface is critical for the subsequent fabrication of the magnetic nanowires.

The silicon wafers with the completed copper wiring were laser diced into one inch square chiplets, each containing ~100 devices. These are stockpiled for subsequent experiments. In this Letter we discuss results obtained by patterning, with electron beam lithography and argon ion milling, 300nm wide, 22 nm thick permalloy ($Ni_{80}Fe_{20}$) nanowires. Figure 2.1 shows a cross sectional diagram of the completed device (a) together with an optical image of the top of the device (b); the Cu lines can be seen in this optical image of the top side of the device through the N-Blok layer. Note that also shown in this device are copper loops for detection of inductive voltage signals. The CMP process requires even fill with metal and dielectric: the arrays of copper dots seen in the image are fabricated for this purpose. On top of the N-Blok layer are the permalloy nanowire (300 nm wide) and three electrical contact pads (only the left 2 are used here). Shown in Figure 2.2 is a cross-section scanning electron microscope image of part of the device. The lower M1 level includes wide copper lines (~35 µm wide in the device shown in Figure 1.1 (b)), which are 400 nm thick. These are used to generate global magnetic fields uniform along the length of the nanowire (0.18 Oe/ mA[ii]). By contrast the upper M2 copper wiring level (150 nm thick) contains a variety of structures. Many of these include series of parallel copper lines with widths and separations of 200 or 400nm. These lines are used to generate large, localized, magnetic fields for the purposes of injecting domain walls into the magnetic nanowires (10 Oe/

[i] A material marketed by Applied Materials under the trade name N-Blok (nitrogen doped barrier low k) which is deposited by PECVD (Plasma Enhanced Chemical Vapor Deposition)

[ii] Fields generated by the M1 and M2 lines are calculated values in the middle of the nanowire. The M1 fields were experimentally verified by comparing the dynamic propagation fields measured using M1 field and an externally applied field.

mA). These lines can also be used to provide tunable dynamic pinning sites along the nanowire (not used here). The magnetic nanowires are aligned perpendicular to the M1 and M2 copper lines.

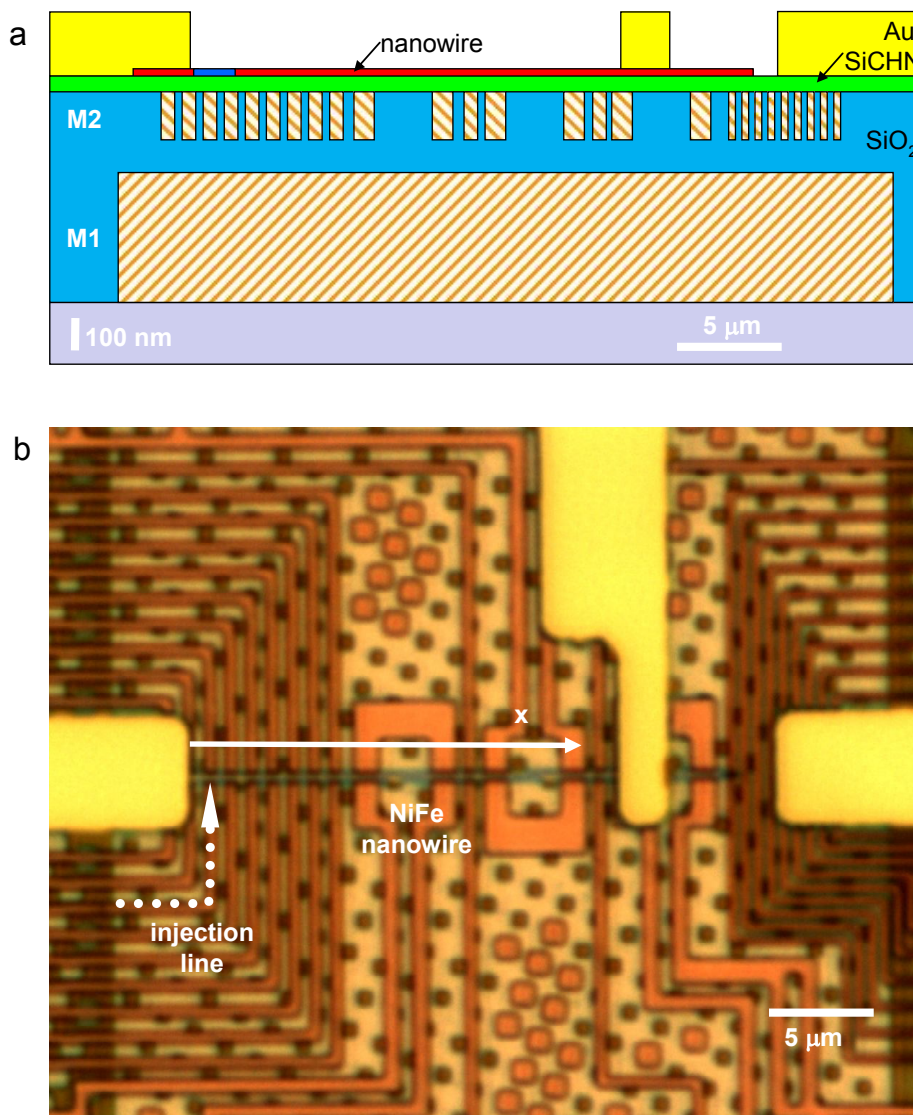Figure 2.1 (a) Schematic cross-section of the device showing: the two levels of copper wires, M1 and M2 (diagonal pattern) buried in SiO_2 and capped with SiCHN with on top the permalloy nanowires (two shades represent the magnetic domains) and gold contacts. (b) Optical image of the top side of the device. The M1 line and the M2 lines (with various widths) in this particular device are drawn in (a) for guidance.
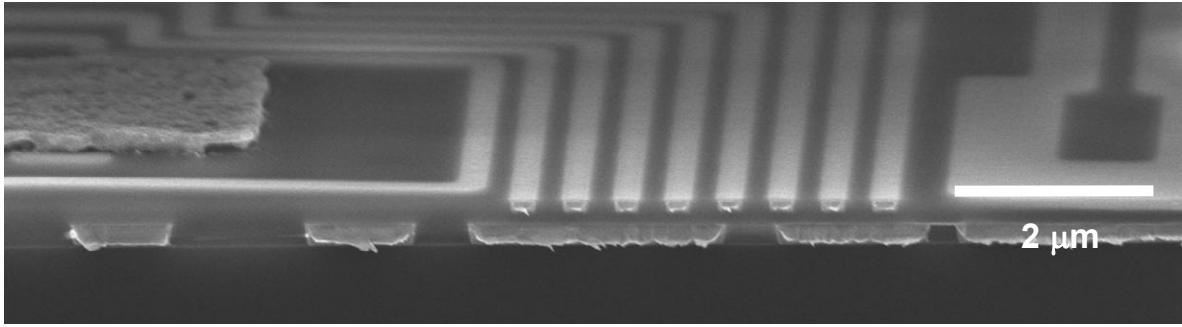
Figure 2.2 A high resolution cross-section scanning electron micrograph of part of a chiplet.

It is important that the vertical separation of the M2 copper wires from the nanowire be as small as possible so as to both maximize the field generated per mA passed through the M2 lines and to provide a sharper field profile. This requires the thinnest possible insulating layer above M2. The use of SiCHN allowed for thinner such layers.

2.3 Pump-Probe Experiments

The domain wall dynamics of the fabricated permalloy nanowires[i] were studied using a pump-probe MOKE technique. Here the "pump" consists of a series of synchronized field pulses generated by passing current pulses through several of the buried Cu lines. The component of the magnetization along the nanowire M_x normalized to the saturation magnetization of the nanowire M_S was probed by its Kerr signal as measured using a pulsed laser diode (wavelength of 440nm, pulses 40ps long, and ~87 pJ/pulse). After passing through a calcite crystal polarizer, a high numerical aperture (N.A. =0.70) objective lens was used to focus the laser beam to a ~400 nm diameter circular spot on the nanowire. The working distance is 6 mm. The beam is incident perpendicularly on the objective lens and after reflection from the nanowire is re-collimated by the same lens. A beam splitter is used to deflect the reflected beam to an analyzer and quadrant diode detector (allowing for measurement of all three magnetization components [78]). An electronic delay generator was used to vary the delay between the pump and probe from 0 to 1200 ns. In Figure 2.3 the setup is shown schematically.

---

[i] The nanowire structure was composed of 0.5 Fe/ 0.3 Al/ 10 Al_2O_3/22 NiFe/ 0.9 Cu/ 4.9 Pt (thicknesses in nm).
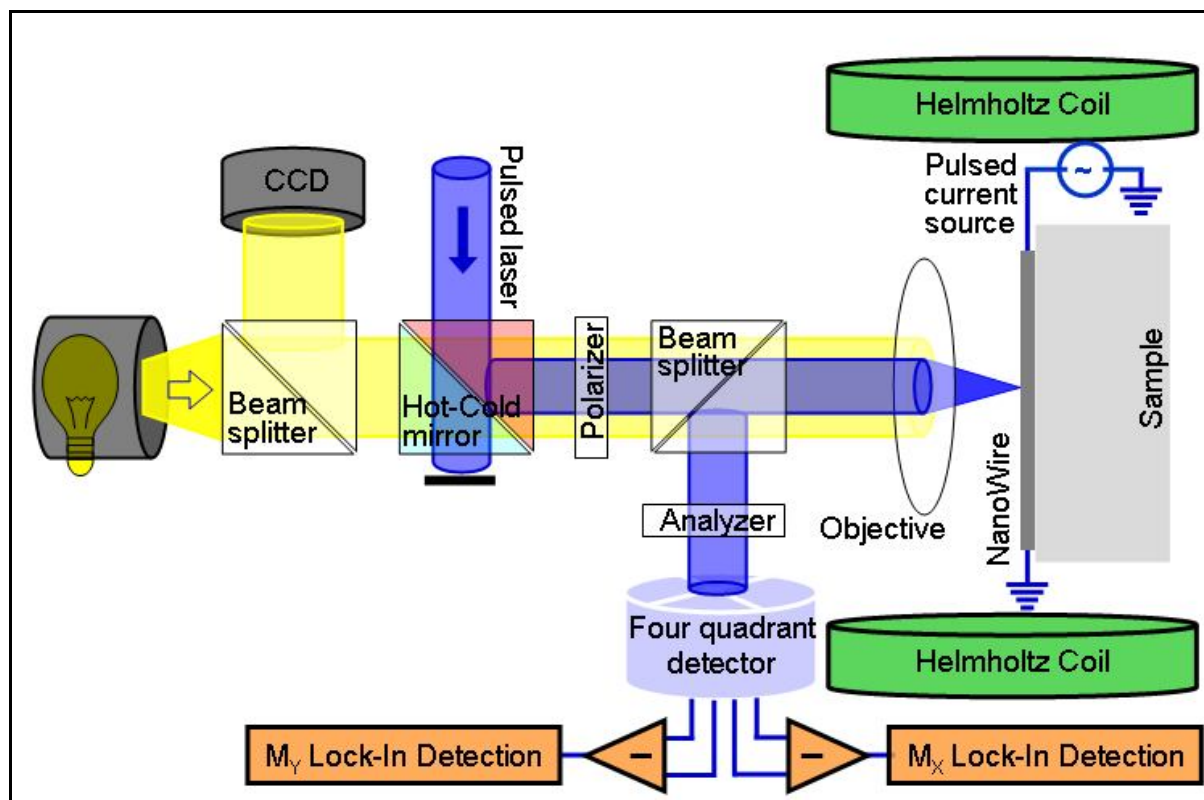
Figure 2.3 Schematic picture of the pump-probe Kerr setup used for time resolved measurements on magnetic nanowires. The sample is mounted on a translation and rotation stage, alignment of the laser beam with the nanowires is obtained by translating the sample while viewing the alignment using a optical microscope that follows the same optical path as the laser beam.

Pump and probe are repeated at a repetition frequency of 781 kHz while the detector bandwidth is limited to 100 kHz. A lock-in detection scheme is deployed by chopping the DW injection pulse (only the first pulse in Figure 2.4 (a)) with a chopper frequency of f_{LI} = 1.1 kHz. The time constant of the Lock-in detector is set to 300 ms. Note that by chopping the DW injection pulse only, the detection method is not sensitive to reflectivity changes caused by temperature changes from current pulses through the nanowire or through the M1 line and only magnetization dynamics caused by an injected DW are measured.
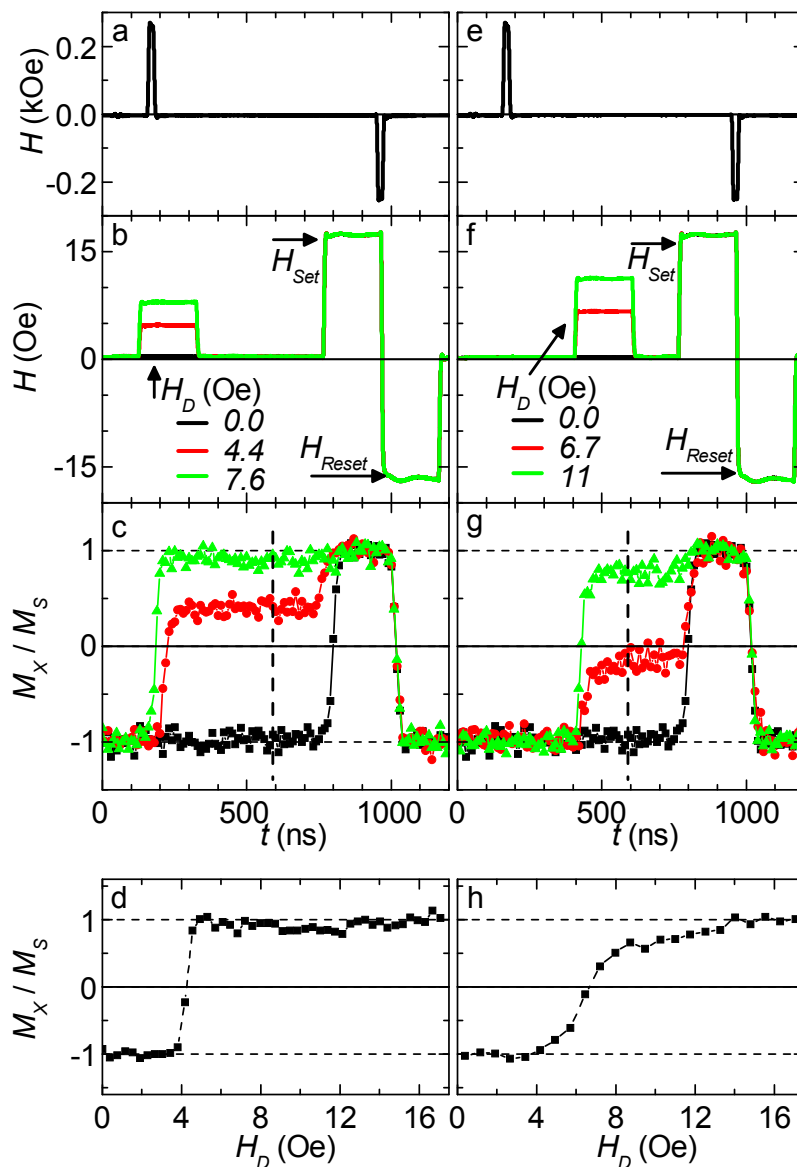
Figure 2.4 (a and e) Time evolution of the DW injection field generated by M2. (b and f) Sequence of global fields generated by M1 used to drive the DW (H_D) and to set / reset the magnetization of the nanowire (H_{Set} and H_{Reset}). (c and g) Time evolution of $<M_x>/M_S$ at x = 8.5 μm. (d and h) Dependence of $<M_x>/M_S$ at x = 8.5 μm and at t = 590 ns versus H_D. (a-d) correspond to dynamic propagation of the DW in which H_D is applied during the DW injection, whereas (e-h) correspond to static propagation of the DW in which H_D is applied 230 ns after the DW injection pulse is completed.

A detailed description of a single pump-probe cycle will now be given with reference to Figure 2.4 (a-c). The nanowire is initially fully magnetized to the left so that $M_x = -M_S$. A current pulse through the M2 injection line is then applied to generate a local field of

+260 Oe (Figure 2.4 (a)) that is large enough to nucleate a domain of reversed magnetization in the nanowire (corresponding to two DWs ~2 μm apart – from MOKE measurements). Simultaneously, a current through the M1 line generates a global driving field H_D along the nanowire (Figure 2.4 (b)). This causes the injected DW to move towards the right end of the nanowire. This pulse is made sufficiently long (200 ns) to allow the DW to propagate along the entire length of the nanowire (if H_D exceeds the propagation field). At some later time (here t = 760 ns) a large field pulse H_{Set} generated by M1 ensures the injected DW propagates to the end of the nanowire if it has not already done so. This allows for normalization of the measured Kerr rotation to that corresponding to M_S. The final step is to reset the magnetic state of the nanowire back to its initial fully magnetized condition using negative field pulses from both M1 and M2 (see the pulses at t = 900 ns in Figure 2.4 (a) and (b)). This field sequence is repeated ~10^6 times to obtain adequate signal to noise in the measured Kerr signal and so to obtain the average value of the normalized component of the magnetization along x, $<M_x>/M_S$.

Figure 2.4 (c) shows the temporal evolution of $<M_x>/M_S$ measured at x = 8.5 μm for three different values of H_D. When H_D = 7.6 Oe, the DW reaches this point shortly after injection so that $<M_x>/M_S$ changes rapidly from $-M_S$ to $+M_S$. However, when H_D = 4.4 Oe the DW takes slightly longer to reach the measurement location, but, more importantly, the magnetization does not switch completely to $+M_S$, but rather attains an intermediate level of only ~$+0.5M_S$. This corresponds to the DW propagating for only a fractional percentage of the repeated pump cycles. Indeed, $<M_x>/M_S$ corresponds to the probability that the DW propagated along the nanowire in a given pump cycle for this drive field. When H_D = 0 the injected DW remains at its injection point so that $<M_x>/M_S$ = 0 until the set pulse is applied. Note that the value of H_{Set} was chosen to be sufficiently large that the DWs would always be driven along the nanowire.

2.4 DW Propagation Field

The detailed dependence of the probability of DW propagation on the drive field is shown in Figure 2.4 (d). Clearly no DW propagation takes place below a critical propagation field H_P^D = 4.2±0.4 Oe above which 100% of the DWs propagate. In these measurements H_D is applied in concert with the injection field pulse so that the DW does not come to rest after injection if $H_D > H_P^D$. This corresponds to a measurement of

the *dynamic* propagation field. The same experiment is repeated in Figure 2.4 (e-h) except that the DW is allowed to come to rest after injection for ~200 ns so that the *static* propagation field can now be measured i.e. the field required to drive an initially stationary DW along the nanowire.

It is clear from Figure 2.4 (d) and (h) that the propagation field of a moving and a stationary DW are distinctly different. The critical propagation field of the stationary DW (~6.5 Oe for 50% probability of motion) is significantly larger and the distribution of the propagation fields is also much broader.

2.5 Current Induced DW Motion

It is now well established that spin polarized current can strongly influence the propagation of DWs via the mechanism of transfer of spin angular momentum (SMT) from the current to the DW [8, 33, 58, 64]. The measurement described in Figure 2.4 can be extended to include the role of current. Figure 2.5 (a) and (b) shows measurements of the dynamic propagation field with and without current applied. Clearly a current of 0.4×10^{12} A/m^2 significantly affects the H_P^D. H_P^D is increased/decreased by ~2 Oe when the flow of spin angular momentum opposes/aids the field driven DW motion. To check that the change in H_P^D arises from SMT rather than the self-field generated by the current flowing through the nanowire the measurement was carried out for both tail to tail and head to head DWs (Figure 2.5 (a) and (b), respectively). Our results are consistent with the SMT mechanism which is independent of the DW type rather than an Oersted field effect which would drive these DWs in opposite directions.

From extrapolation of the data in Figure 2.5 current induced DW motion would take place in zero field at a current density of $\sim 0.9 \times 10^{12}$ A/m^2, consistent with our previous studies using AMR [60, 79]. However, the nanowire was not able to withstand such high current densities because it became too hot. The poor thermal conductivity of the relatively thick dielectric layers used to fabricate the buried Cu lines results in significant heating of the nanowires.
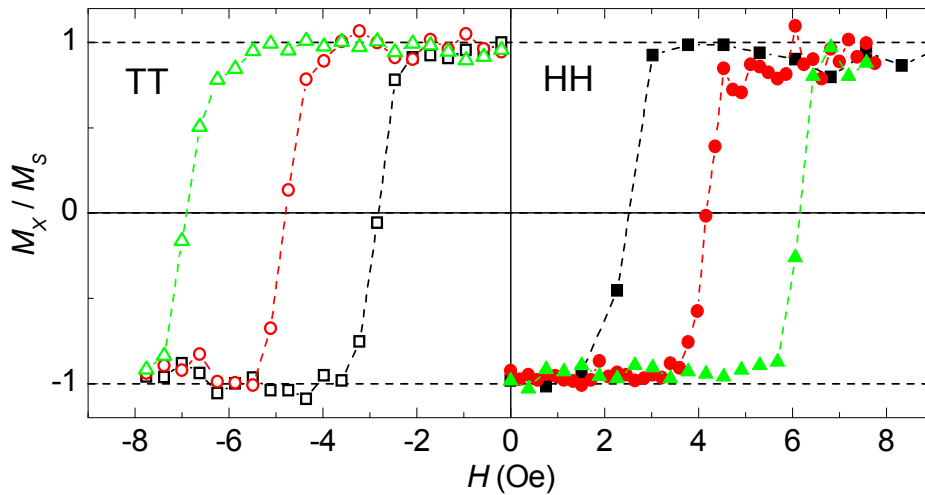
Figure 2.5 Influence of current on dynamic propagation of DW. $<M_x>/M_S$ versus H_D when $J = 0$ (discs), -0.4×10^{12} A/m^2 (squares) and $+0.4 \times 10^{12}$ A/m^2 (triangles). The current is simultaneously applied with the drive field. Data are shown for tail to tail (TT) DWs (open symbols) and head to head (HH) DWs (closed symbols).

2.6 Joule Heating

The temperature of the nanowire can be measured in real time from the magnitude of the Kerr signal of the fully magnetized wire. When the nanowire is heated M_S and the corresponding Kerr signal is reduced. Assuming a linear relationship between these quantities the temperature of the nanowire was obtained by first measuring the temperature dependence of the magnetization of a permalloy film of the same thickness as the nanowire. As shown in Figure 2.6 (a) a 20 ns long current pulse was applied to the nanowire when its magnetization had been switched to $M_x = +M_S$. The resulting Kerr signal converted to temperature is shown in Figure 2.6 (b). A significant increase in temperature of ~300 $^{\circ}$C is reached in 20 ns. This is about the maximum temperature obtainable without destroying the nanowire. When a current pulse of higher magnitude or duration is applied an avalanche of increased resistance and increased power dissipation will quickly burn the nanowire when these pulses are applied at high repetition rates.
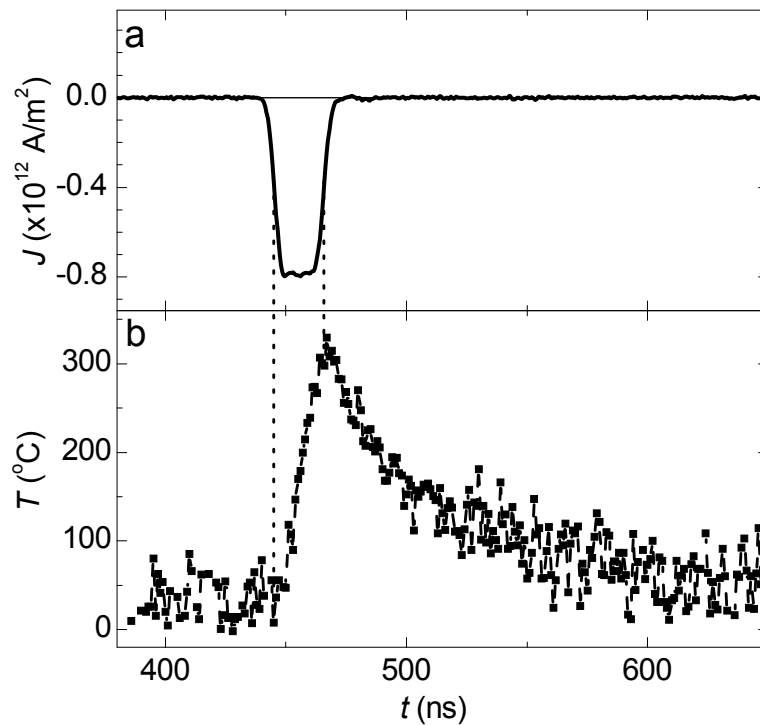
Figure 2.6 Temperature of nanowire inferred from magnitude of Kerr signal during application of a current pulse. (a) 20 ns long current pulse of magnitude -0.8×10^{12} A/m^2 is applied to the nanowire after the magnetization has been reversed using the field sequence shown in Figure 2.4 (a-b). (b) Inferred temperature transient.

2.7 Resolving Components of the Magnetization Vector

One of the interesting capabilities of pump-probe Kerr microscopy is resolving the different components of the magnetization vector. In order to achieve such a vectorial resolution we used a configuration with a four quadrant detector, as introduced in chapter 2.3. An example of such a measurement, resolving the magnetization components in the film plane (x and y) and perpendicular to it (z), is shown in Figure 2.7 (a,b,c). The black curve shows the magnetization transient measured when a propagation field is applied high enough to propagate the DW throughout the nanowire. M_x switches completely once the DW passes the detection spot at $t = 250$ ns and switches back at $t = 730$ ns when the wire is reset. No signal is visible in the M_y and M_z direction since the nanowire is purely magnetized along the wire and the DW moves too quickly to pick up the DW structure's off axis magnetizations.

Next a field is applied locally at the position of the detection spot by passing a current through one of the M1 level wires. This local field serves as a pinning field and is large enough to withhold further propagation of the DW. The DW injected at one end of the wire will now propagate through the wire until it reaches the detection location were it will be stopped by the local pinning field. The moving DW structure will have a finite canting out of the plane (ψ) as predicted by the 1D model. When now suddenly the DW propagation is stopped by the local pinning field, relaxation of the internal DW magnetization structure causes the DW to move backwards. The mechanical analogon of this, as discussed in chapter 1.3.3, is that the DW carries a finite Mass, the Döring Mass, and thus has a finite momentum. When the DW enters the local region with opposed field (the pinning field) its velocity will gradually be reduced until it has been stopped completely. Due to this momentum of the DW it is able to penetrate deeper into the local field than it would in the quasi static case. Once the DW is stopped it will be accelerated again in the opposite direction and eventually find an equilibrium position between the global applied field and the local applied pinning field.

The transient marked with discs in Figure 2.7 shows the magnetization as measured at the position of the local pinning field when a pinning field is present. The magnetization transient along the wire (M_x) shows that the DW first passes the measurement position, registered as a complete switch from $-M_S$ to $+M_S$ at $t\sim 250$ ns. Then 75 ns later M_x reduces again to about $+0.25M_S$, this can only be caused by a DW that is moving backwards. If the DW moved back out of the measurement location completely, the magnetization M_x measured locally would completely switch back to $-M_S$. Here M_x does not switch back completely which is interpreted as a DW that is stopped at a position that at least partially overlaps with the measurement spot.

Now that the DW is pinned at the measurement position, part of the internal DW magnetization structure is exposed to the measurement. Since a vortex structure DW is expected in nanowires of the width and thickness used here (300×22 nm), part of the nanowire magnetization is expected to locally point in the direction perpendicular to the nanowire. Moreover, the core of the vortex DW structure is a tiny region of about 5 nm diameter where the magnetization points out of the plane. Indeed a non zero signal is obtained for the M_y transient in the timeframe the DW is confined at the measurement position, as shown in Figure 2.7 (b). The out of plane component of the magnetization M_z, plotted in Figure 2.7 (c), is not visible, even in this case were the DW is positioned

statically at the probe laser spot. Probably the core of the vortex, the only part of the DW that contains out of plane magnetization, is too small to be seen by this technique.
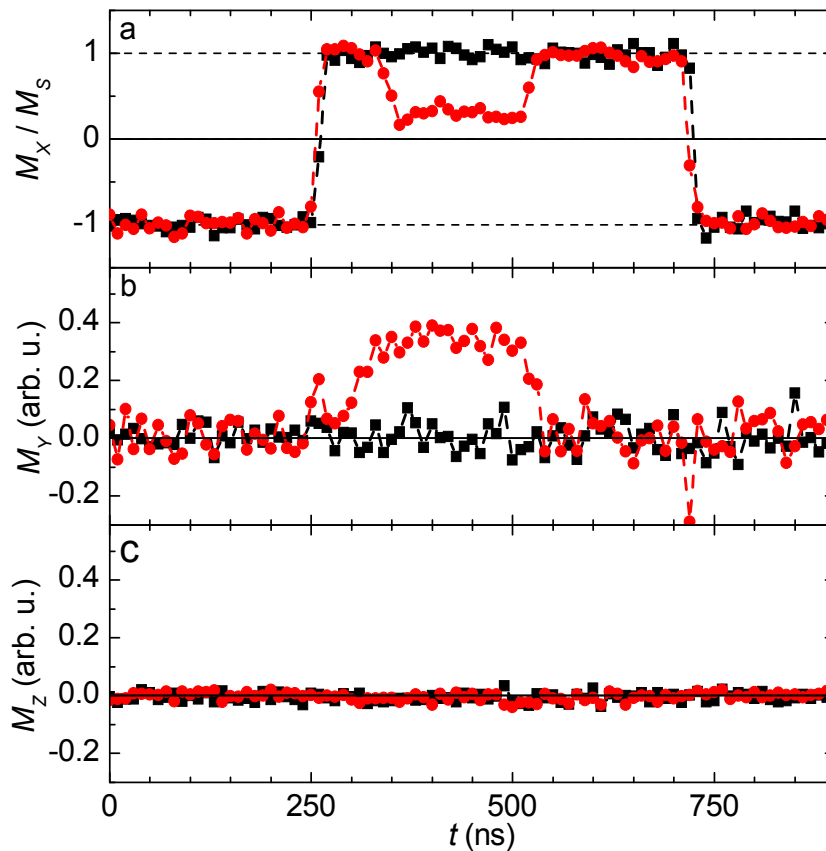
Figure 2.7 Magnetization transient measured when no pining field is present (squares) and when a pinning field is present (discs), measured locally at the pinning field position, for the three vectorial components of *M*: along the nanowire (a), perpendicular and in the plane (b) and perpendicular out of the plane (c).

2.8 Conclusion

In summary, we have developed a technique for generating large local magnetic fields at MHz rates using two levels of copper metal lines buried close to the surface of a silicon wafer. Current pulses passed through these lines are used to generate magnetic fields locally or globally along magnetic nanowires fabricated on the surface of the patterned wafer. These fields are used to both inject and drive domain walls along the nanowires. Using this novel device, together with a pump-probe MOKE detection scheme, we have demonstrated that the static and dynamic propagation fields of domain walls in permalloy nanowires are substantially different.

C h a p t e r   T h r e e

Domain Wall Propagation Field

An investigation of the static and dynamic domain wall

propagation fields in permalloy nanowires[i]

Pump-probe Kerr microscopy is used to measure the dynamic and static domain wall propagation fields in permalloy nanowires. The dynamic propagation field is found to be significantly smaller than the static propagation field, which can be accounted for within a one-dimensional analytical model when a simple form of roughness is introduced. The static propagation field shows a subtle dependence on details of the nanowire's imperfections and the domain wall injection procedure.

3.1 Introduction

Fundamental understanding of the field and current driven motion of domain walls in magnetic nanowires is of critical importance to the development of recently proposed domain wall based memory [8] and logic devices [65]. Of particular importance is the role of imperfections in the nanowire devices on the motion of the domain walls (DWs) [59, 80, 81]. These directly influence the magnitude of the critical threshold field needed for DW propagation. It has previously been shown that this threshold field is distinctly different for inducing the motion of initially stationary DWs compared to that needed to drive DWs, that are already in motion, along the same nanowire [80]. In this chapter we use pump-probe Kerr microscopy in conjunction with simple analytical models to show the subtle dependence of the static propagation field on details of the nanowire's structural imperfections.

3.2 One Dimensional Model

A useful and simple one-dimensional (1D) model for understanding DW dynamics was developed in the 1970s to understand field driven DW dynamics [30] (cf. chapter 1.3.3). This model has been extended in recent years to include the current induced motion of DWs via the mechanism of spin momentum transfer [14, 16, 35, 36]. The basic assumption of the 1D model is that the DW structure does not fundamentally change as the DW propagates. Thus, the DW can be described by just two parameters, x and ψ, where x is the position of the DW along a nanowire and ψ is the out of plane angle of the local magnetization within the DW structure.
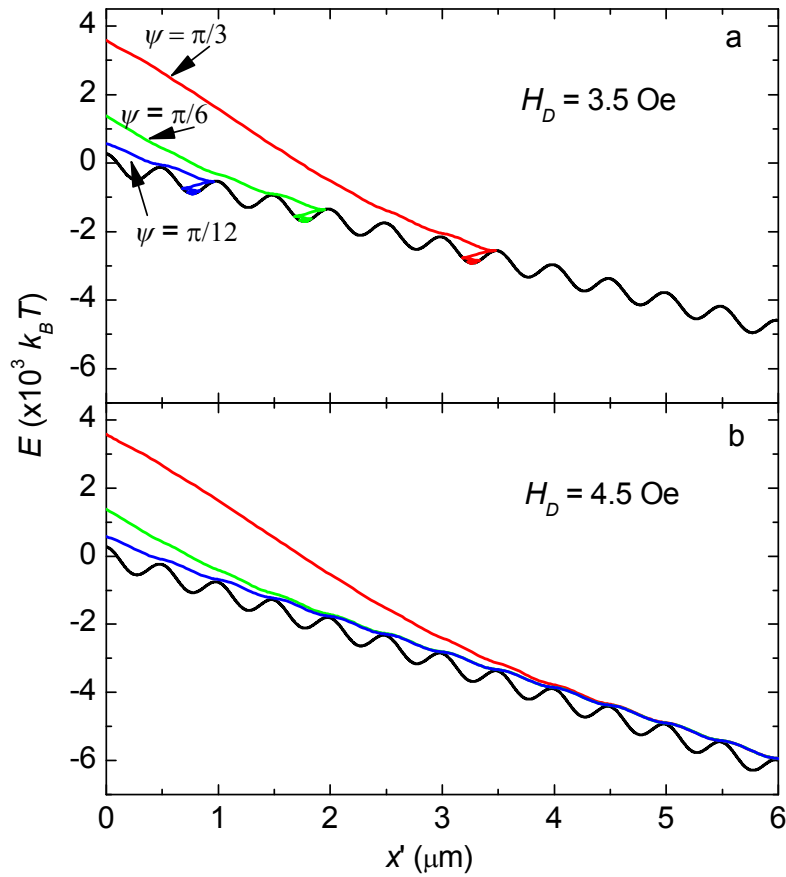
Figure 3.1 one dimensional model calculation of the spatial dependence of the energy of a DW injected into a permalloy nanowire (of cross-sectional area 300×20 nm) in the presence of a sinusoidally varying energy potential V (black line). V has an amplitude of 277 $k_B T$ with a period $\lambda = 500$ nm. The static de-pinning field is $H_P^S = 15$ Oe. For three initial DW angles ψ at position $x = 0$. The DW is driven by a field of strength 3.5 Oe and 4.5 Oe in (a) and (b), respectively.

We first use the 1D model to illustrate that the dynamic DW propagation field is distinct from the static propagation field when the nanowire has an inhomogeneous magnetic structure, for example, due to roughness along its edges or surfaces. The length scale of roughness relevant to DW motion is of the order of the DW width. Shorter length scale variations will be integrated out over the DWs width. Thus, we consider an energy potential that varies sinusoidally along the nanowire so that the DWs energy at rest can be written as a combination of this potential energy term plus a Zeeman energy term as follows:

$$E_P = 2MSHAx + V\cos\left(2\pi\frac{x}{\lambda}\right). \qquad (3.1)$$

M_S is the saturation magnetization, V and λ are the amplitude and wavelength, respectively, of the sinusoidal potential, and A is the cross sectional area of the wire. We ignore the Zeeman energy of the DW itself since this is constant in the 1D model during the DWs motion (for fields applied along the length of the nanowire).

A DW at rest will be trapped at one of the local energy minima. The propagation field to move this DW is found by calculating the strength of the field at which the energy potential landscape is sufficiently tilted that its energy barrier vanishes. Thus, the threshold field to move a static DW is given by,

$$H_P^S = \frac{\pi V}{\lambda M_S A}. \qquad (3.2)$$

By contrast, a moving DW, which has momentum, can overcome the same potential barrier at a lower propagation field, as illustrated in the model calculation shown in Figure 3.1. The parameters are chosen to correspond to a permalloy nanowire [14] (with the Gilbert damping parameter, $\alpha = 0.01$, the dynamic DW width, $\Delta = 20$ nm, and the shape anisotropy field, $H_K = 1900$ Oe) with $H_P^S = 15$ Oe (see below) and $\lambda = 500$ nm. We use the 1D model, as discussed in chapter 1.3.3, to calculate the trajectory of a DW which has enough initial momentum (as characterized by its canting angle ψ) or potential energy (by varying its initial starting position x) to overcome the first barrier. We find that such a DW, which we call a dynamic DW, can be driven completely along the nanowire when a minimum field, the dynamic propagation field, of $H_P^D \sim 4.1$ Oe is applied. This is clearly much lower than H_P^S. Examples of driving fields just above and just below H_P^D are shown in Figure 3.1. At $H_D = 3.5$ Oe (Figure 3.1 (a)) the DW will eventually be trapped at a distance along the nanowire which increases with ψ whereas at a driving field of $H_D = 4.5$ Oe (Figure 3.1 (b)) the DW propagates along the nanowire indefinitely.

3.3 Experimental

A novel pump-probe scanning Kerr microscopy technique is used to characterize the static and dynamic propagation fields of domain walls injected into a permalloy nanowire with a cross-sectional area of 300×20 nm^2 and a length of ~15 μm. This

experiment uses local magnetic fields generated from currents passed through copper lines buried beneath the nanowire as introduced in chapter 2.2. The use of these buried lines, fabricated using a 180 nm CMOS process, allows the generation of local and global fields at high repetition rates (MHz). This allows the Kerr signal to be accumulated in a reasonable amount of time with sufficient signal to noise. The component of the magnetization along the nanowire, M_x, normalized to the saturation magnetization of the nanowire, M_S, is inferred from the Kerr signal. A single experiment consists of measuring $<M_x>/Ms$ at a fixed point along the nanowire 420 ns after a DW is injected into the nanowire. The measurement position x is varied in successive experiments. The nanowire is first magnetized along the $-x$ direction so that $M_x = -M_S$ at the measurement point. A DW is then injected and the Kerr signal measured to determine if the DW has reached the measurement point. The DW injection is accomplished by applying a localized field pulse to a region of the nanowire. The field (~200 Oe) is generated by passing a current pulse (20 ns long) of appropriate strength and direction through one of the buried lines.

3.4 Results and Discussion

In a first set of experiments shown in Figure 3.2 the position along the nanowire of a DW injected in the presence of a small global bias field H_{bias} is determined by varying the measurement position x. The local field from the buried line has a spatial profile along the nanowire as shown in the calculation in Figure 3.2 (a,b). The injected DW will be driven along the nanowire until the local field drops below H_P^D. By adding a small bias field the DW will be driven further along the nanowire until again the net local field falls below H_P^D. In this way the position of the DW along the nanowire from the injection point can be varied. This is confirmed by pump-probe Kerr measurements as a function of distance along the nanowire after injection of a DW.
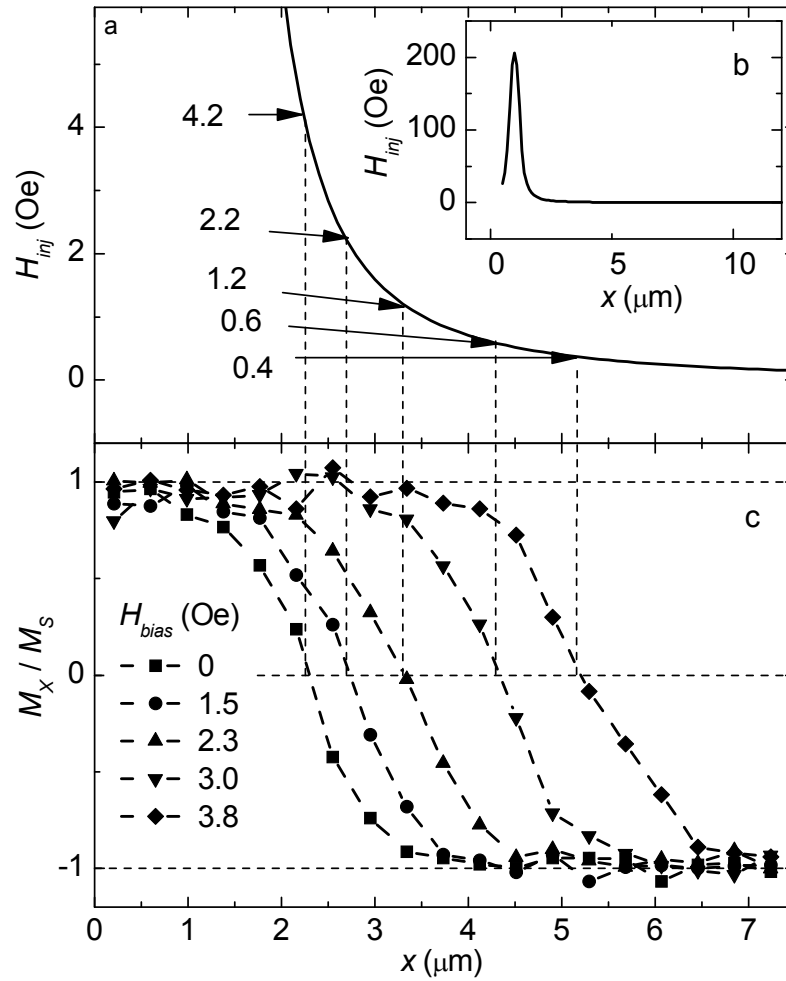
Figure 3.2 (a,b) Calculated spatial variation along the nanowire of the injection field from a current pulse of magnitude 21.7 mA applied through the injection line. The distance x is measured with respect to the edge of one of the current contacts to the nanowire. The injection field arises from a Cu line of width 400nm, and thickness 150nm, buried 50nm beneath the surface of the chip. Note that the middle of the injection line is at $x = 1$ μm. (c) Variation of the normalized in-plane magnetization along the wire after a DW has been injected in the presence of a small global bias field along the nanowire, measured with scanning Kerr microscopy.

Figure 3.2 (c) shows $<M_x>/M_S$ as a function of x for various bias fields. The probability that the DW has passed beyond the distance x is given by $(1-m)/2$, where $m = <M_x>/M_S$. When $m = 0$ there is a 50% probability that the DW has passed this position. Using this criterion to define the position of the DW the experiments clearly show that the position

x_i of the injected DW from the injection line increases with increasing bias field. When H_{bias} exceeds H_P^D the DW propagates to the end of the nanowire (data not shown).
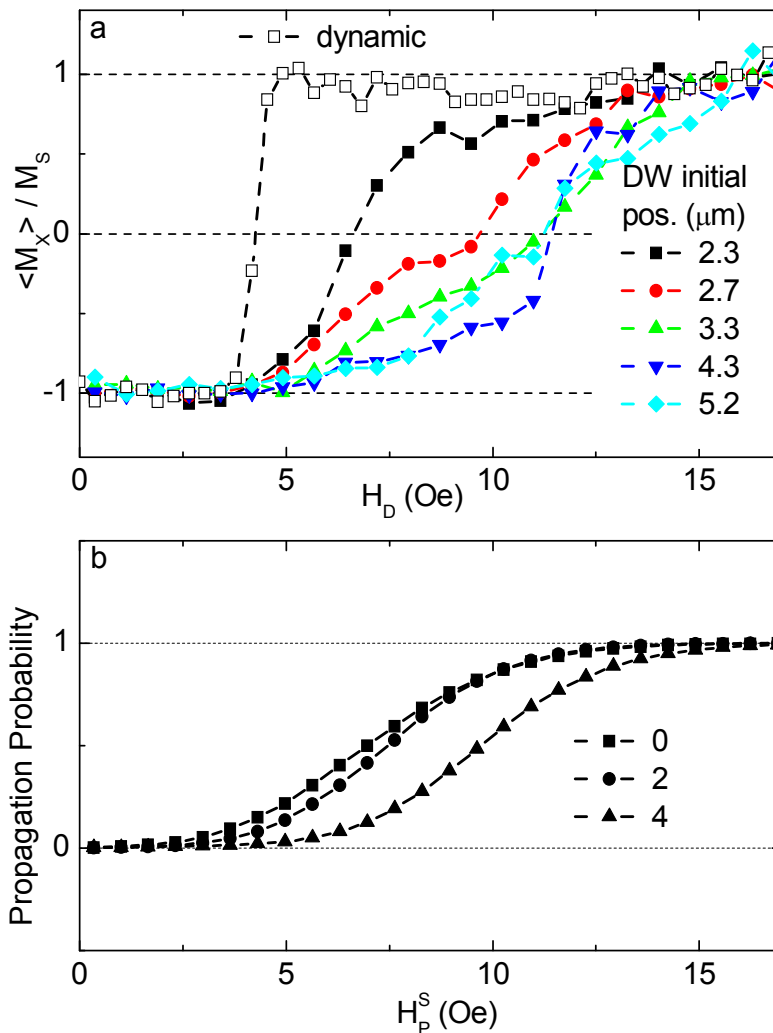
Figure 3.3 (a) Average normalized magnetization at a fixed position $x = 8.5$ μm along the nanowire measured after the application of a drive field H_D for DWs at the initial positions indicated (solid circles) and also for the dynamic case. The magnetization is averaged over $\sim 10^6$ repeated experiments in each case. (b) Model of the probability distribution of the static propagation field of DWs injected into many simulated random energy landscapes using the bias fields shown, as discussed in the text.

In the next set of experiments the dependence of the propagation field on the initial position of static DWs is determined. This is accomplished by measuring m at a fixed position along the nanowire far from the injection line ($x = 8.5$ μm) as a function of drive field H_D as shown in Figure 3.3 (a). When the drive field exceeds the propagation

field then the magnetization will be reversed at the measurement point. Thus, here $(1+m)/2$ is the probability that the DW has travelled beyond the measurement point. As can be seen from Figure 3.3 (a), a broad transition of the probability with drive field is found; the probability that the DW reaches the measurement point increases gradually from zero for $H_D \sim 5$ Oe to $\sim 100\%$ for $H_D \sim 15$ Oe. The details of this transition sensitively depend on the initial position of the DW. Perhaps surprisingly, when the initial position of the injected DW is further from the injection line, the static propagation field is increased. This effect is caused by the DW injection mechanism that favors deeper pinning locations when a higher field is applied (see below).

By contrast with the propagation of static DWs, a much sharper transition is found for dynamic DWs (see Figure 3.3 (a)). In the latter case the DW is injected into the nanowire in the presence of a drive field so that when the drive field exceeds H_P^D the DW never comes to rest before reaching the measurement point. The dynamic propagation field is well defined with $H_P^D \sim 4.2$ Oe.

The simple model in Figure 3.1 cannot account for the observed sensitivity of H_P^S on x_i since the energy minima in the model are identical so that no matter where the DW initially resides the same field is required to propagate a static DW. In order to account for our experiments we need to include random fluctuations in the depth and spacing of the energy minima. We use a randomly generated sequence of numbers within a Gaussian distribution to represent the energy along x, $E(x)$. We filter out the Fourier components that are much smaller and larger than the physical DW width [22] (here, chosen to be 150 nm and 800 nm, respectively) so as to obtain a representative DW energy potential landscape for a rough nanowire as shown in Figure 3.4 (b).
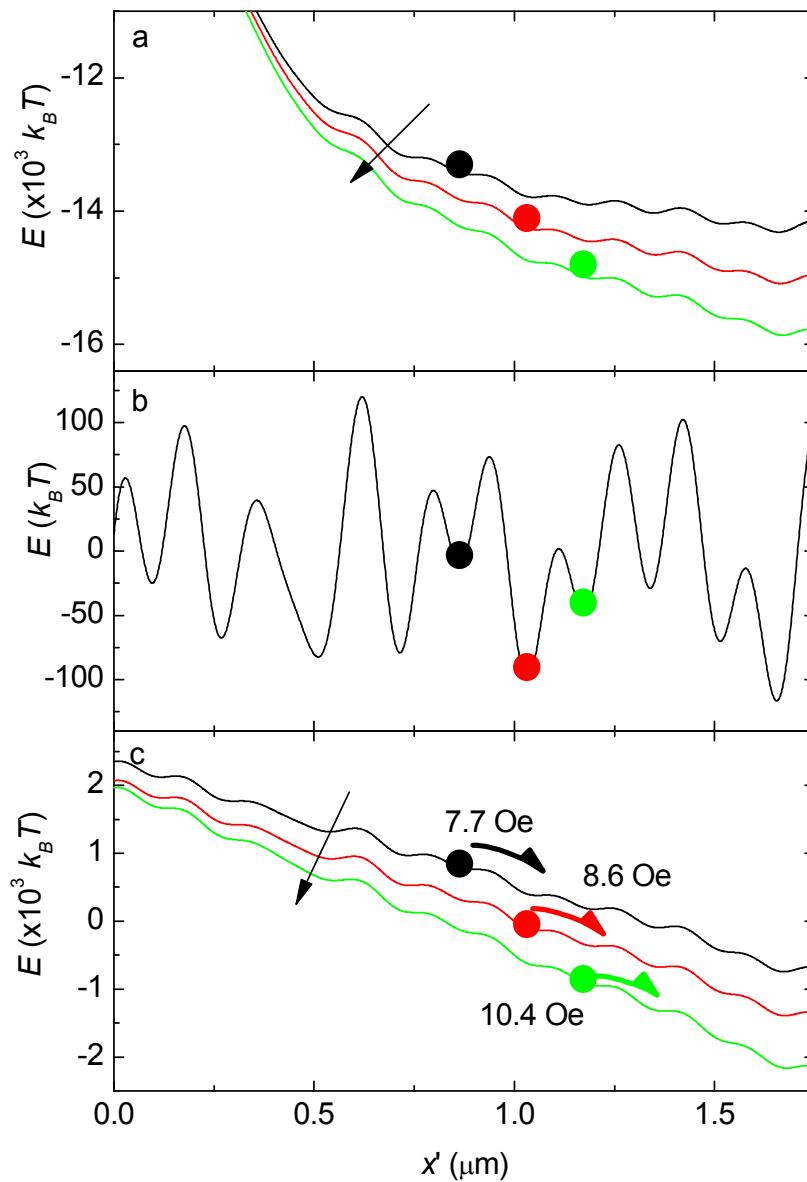
Figure 3.4(a) Domain wall energy in a simulated energy landscape (see text) including the injection field, for bias fields of 0, 2 and 4 Oe, increasing in the direction of the arrow. Solid circles indicate the position of the first local minimum in the energy landscape where the DW will be initially pinned. (b) Energy landscape after the injection and bias fields are switched off. (c) Energy landscape in the presence of the field required to propagate the DW.

The DW energy landscape is modified during the DW injection process by the combination of the local injection field (Figure 3.2 (b)), and the global bias field, as shown in Figure 3.4 (a). These fields tilt the energy landscape with a slope which is greater the closer the DW is to the injection point. This means that statistically the smaller the bias field the smaller the number of energy minima that the DW will on

average sample so that it tends to be trapped in a less deep energy well. This is illustrated in Figure 3.4 (a) for DWs injected at $x' = 0$ into the same rough energy landscape but in varying bias fields of 0, 2 and 4 Oe. (x and x_i in the measurement refer to the position relative to the edge of one of the current contacts to the nanowire, x' in the simulations refer to the position relative to the injection line; injection in the measurements is done at $x \sim 1$ µm). Assuming that the injected DW is trapped at the first local minimum that it encounters the position of the DW at rest is indicated by the solid colored circles in Figure 3.4 (a). When the bias and injection fields are removed the DW energy landscape is that of Figure 3.4 (b). The static propagation field is then found from the strength of the field needed to tilt the landscape so that the energy barrier trapping the DW vanishes. These fields and the corresponding energy landscapes in the presence of these propagation fields are shown in Figure 3.4 (c).

The method of Figure 3.4 is repeated for many randomly generated energy landscapes so that the probability distribution of the calculated static propagation fields can be found, as shown in Figure 3.3 (b). These distributions have the same characteristic features as the measurements shown in Figure 3.3 (a). The model correctly predicts that the static propagation field is increased when an increased bias field is applied during injection as is experimentally observed. This is because the DW has a greater chance of finding a deeper energy minimum the greater the bias field.

3.5 Conclusion

In conclusion, both experiments and a simple 1D analytical model clearly reveal that the propagation field of a moving DW is significantly smaller than that of a DW at rest in the same energy landscape. Moreover, an interesting dependence of static propagation field on small global bias fields applied during the injection of a DW into a permalloy nanowire from a local field was found. This could be accounted for by simulations of a rough nanowire. The DWs that sample a greater number of local energy minima come to rest within a deeper energy minimum on average. Our experiments reveal how subtle is the dependence of the propagation field of a DW on the imperfections of a nanowire.

Gilbert Damping

Field driven domain wall dynamics in magnetic nanowires when Gilbert damping is varied[i]

Field driven magnetic domain wall dynamics in permalloy nanowires is explored as a function of Gilbert damping, by changing the concentration of osmium doping. Apart from controlling the domain wall velocity, we show that it is possible to modify the minimum field needed to maintain the propagation of domain walls in the nanowires. This dynamic propagation field is found to increase when the Gilbert damping increases. Measurements are then compared with a simple model for nanowire roughness. Good agreement is obtained when also the reduction of the magnetic moment and the reduction of the exchange interaction due to the osmium doping is taken into account.

4.1 Introduction

Study of the dynamics of domain walls (DWs) in magnetic nanowires is of high interest since novel applications for memory and logic based on DW motion have been proposed [9, 65, 66]. In most of these proposals DW motion driven by current, through the spin momentum transfer effect (SMT), rather than field is elemental. However a fundamental problem with current driven DW motion to date is the high current density needed to accomplish DW motion [14]. One possible solution is believed to lie in the fabrication of magnetic materials possessing just that other set of magnetic properties that favors lower current SMT. Although most work on DW dynamics in magnetic nanowires is concentrated on permalloy much work has also been done on other materials [61, 82-85] and theoretical models are now evolving [36, 48, 86]. In an effort to validate existing models beyond permalloy and to search for magnetic properties of importance to SMT we here report of the measurement of DW dynamics in a permalloy nanowire samples series with increasing Gilbert damping.

Contrarily to what one could naively think, damping is a necessity for field driven DW motion. No DW motion will take place in a system with zero damping, instead the magnetic moments, or the DW structure as a whole will precess in the applied field. In that sense, thinking of magnetization damping as some sort of viscosity (as introduced in chapter 1.3.2) is rather misleading. Moreover the maximum velocity of a field or current driven DW propagation is independent of the Gilbert damping α. The DW needs to dissipate the excess energy gained from the applied field as Zeeman energy, and the only avenue to do so is through magnetization damping. At higher applied fields a higher rate of dissipation is needed, hence a larger canting angle of the magnetization out of the plane. When no further canting is possible, $\psi = \pi/2$, the DW structure starts to precess, the onset of this DW velocity regime is marked as the Walker breakdown field. Larger Gilbert damping will thus postpone the Walker breakdown to higher applied fields and can therefore be of advantage for the controllable motion of DWs.

We will vary the osmium concentration in permalloy nanowires in order to obtain increased Gilbert damping. This osmium doping causes, besides improved Gilbert damping, also changes in the other magnetic properties of the material. Measurements of the full field driven DW velocity profile, $v(H)$ will than be compared with the 1D model for DW propagation. For this comparison to be successful special caution needed to be taken in order to correctly incorporate the changes in all magnetic material

properties. Finally we show a measurement of the minimum field need to maintain field driven DW propagation, the dynamic propagation field H_p^D. The measured value of H_p^D is in good agreement with the model, moreover the same model also predicts the behavior of H_p^D when the Gilbert damping increases.
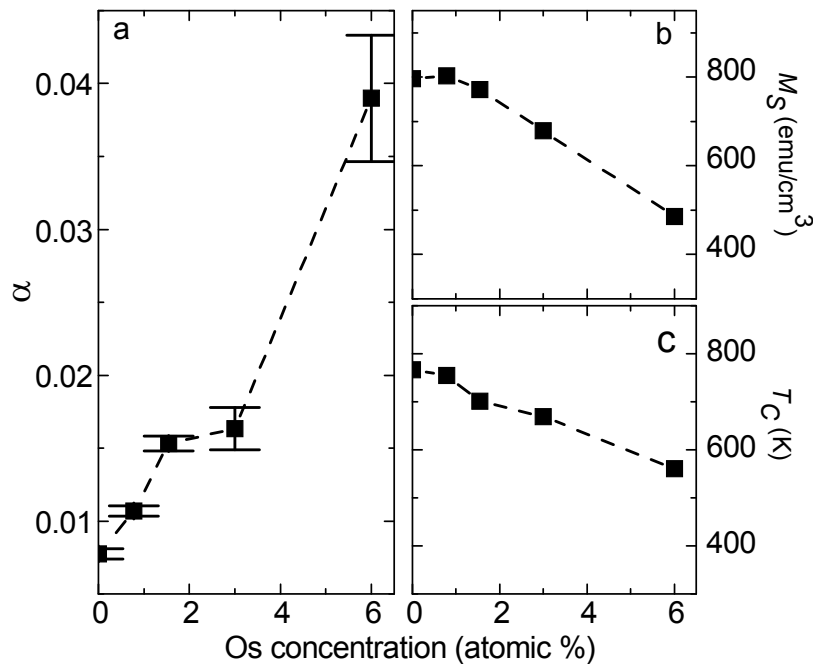

Figure 4.1 Dependence of the magnetic properties of 22 nm thick permalloy films on osmium doping: strip-line FMR measurement of (a) the Gilbert damping parameter, α, and (b) saturation magnetization, M_S, at room temperature and (c) VSM measurements of the Curie temperature, T_C.

4.2 Sample Fabrication and Magnetic Material Properties

Gilbert damping in permalloy can be effectively increased by doping thin films with osmium [87]. Therefore a sample series of 20 nm thick permalloy films with increasing atomic concentrations of osmium ranging from 0.0% to 6.0% has been prepared using magnetron sputtering deposition. Varied osmium concentrations are obtained by alternating layers of 1 nm thick Ni/Fe(80/20) with layers of Ni/Fe/Os(78.6/18.4/3.0) or Ni/Fe/Os(75.2/18.8/6.0). The atomic concentration of osmium in the so obtained sample series has been verified using particle induced X-ray emission (PIXE). Strip line ferromagnetic resonance (FMR) [88] is used to determine the Gilbert damping in the continuous films. Figure 4.1 shows the measured Gilbert damping, parameterized by the

dimensionless parameter α, versus the measured osmium concentration in the permalloy films; Gilbert damping increases 5 times over the osmium doping range. The Curie temperature, T_C, is reduced due to the replacement of nearest neighbors by Os atoms. A measurement of T_C using a vibrating sample magnetometer (VSM) with controllable temperature is shown in Figure 4.1 (c). As witnessed by the reduction in T_C, also the exchange energy, A, is suppressed by doping the permalloy films with osmium, since the onset of ferromagnetic order happens when thermal and exchange energy are of comparable magnitude. Finally also the saturation magnetization, M_S, is suppressed directly by the Os doping itself and indirectly by the increase of the relative temperature T/T_C when measured at a fixed temperature (293 K). Figure 4.1 (b) shows the strip line FMR measurement of M_S in the continuous films.

After deposition on a prefabricated CMOS chip to produce localized field pulses, as discussed in detail in chapter 2.2, 300 nm wide, straight nanowires are patterned in the osmium doped permalloy films using electron beam exposure and oxygen reactive ion etching.

4.3 Experimental

Magneto optical Kerr effect microscopy (MOKE) has been utilized in a pump-probe setup to measure the passage of a DW locally at various positions along the nanowire as described in detail in chapter 2. A DW is injected into the nanowire at one end by a highly localized field pulse of 20 ns duration. At the same time a field, H, is applied homogeneous over the full length of the nanowire to propagate the newly injected DW throughout the nanowire. The Kerr measurement is performed by focusing a laser to a ~400 nm spot onto the nanowire at a position x along the nanowire. The passage of the DW will now be registered as a change in the local magnetization and thus in a change in polarization of the reflected light with a time resolution of ~1 ns.

The time of passage, t, together with the position, x, on the nanowire reveals the DW velocity when a field of strength H is applied. Figure 4.2 (a) shows the measurement of $x(t)$ for 5 different applied fields in permalloy with 0.8% Os doping, clearly the DW moves at a constant speed over the measured region in the nanowire. Linear fitting to the data results in a DW velocity profile $v(H)$. Repeating the same measurement of $v(H)$ on permalloy nanowires with varied osmium doping then results in the velocity profiles shown in Figure 4.2 b. The DW velocity increases linearly with applied field up to a

certain field known as the Walker breakdown field, H_{WB}, where the velocity reaches its maximum, v_{Max}. Because the rate at which a moving DW can dissipate Zeeman energy through Gilbert damping is limited, further increase in applied field will not further increase the DW velocity. Instead the internal magnetization structure of the DW starts to oscillate causing a decrease in propagation velocity.
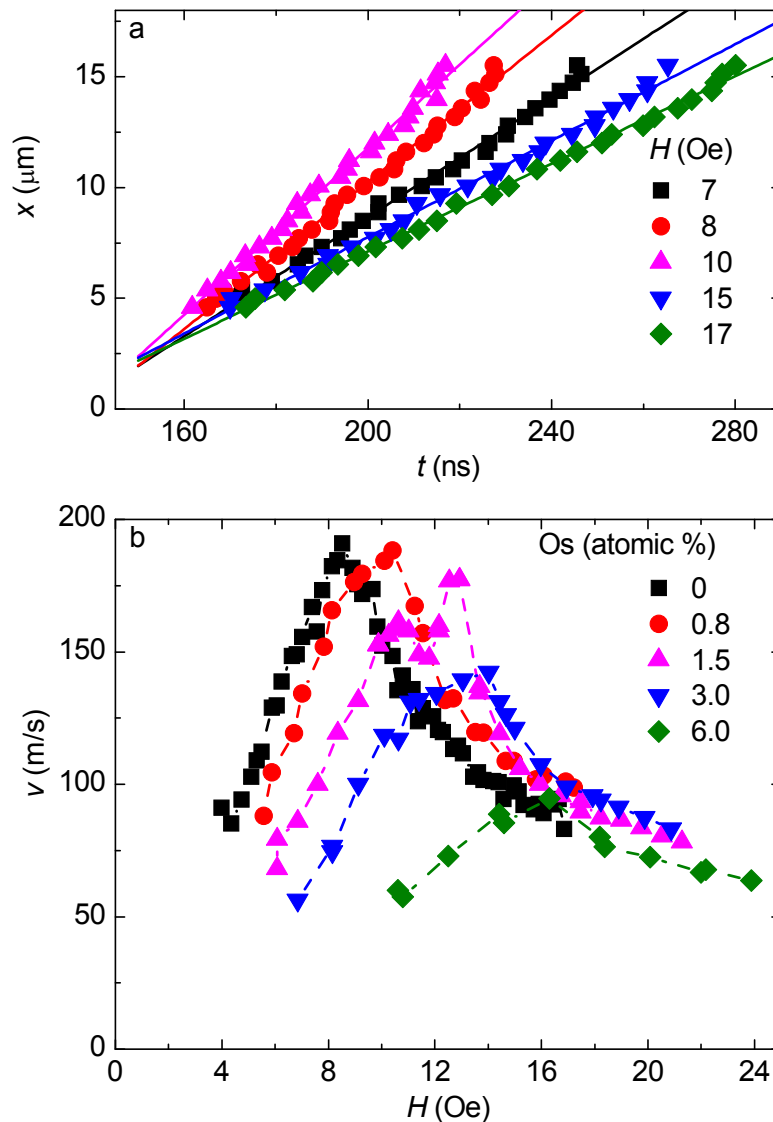
Figure 4.2 (a) DW position x along $Py_{1-y}Os_y$ nanowire for $y = 0.8\%$ versus transition time t for several applied fields (symbols). The lines are linear fits to the data. (b) Field driven DW velocity versus applied field for a series of nanowires for various Os doping concentrations y.

4.4 One Dimensional Model

The one dimensional model (1D model) for DW motion describes a Bloch DW in a one dimensional magnetic wire [30] as a rigid particle with only two properties: the DW

position, x, in the nanowire and the canting angle out of the plane, ψ, of the local magnetization inside the DW, see chapter 1.3.3. Owing to its simplicity the 1D model has been used for higher dimensional systems. In order to account for the lowered energy of the different DW structure expected in such wider geometries the anisotropy, H_K, and DW width Δ have been reformulated into effective parameters [14, 24]. Assuming stationary DW motion, $\dot{\psi} = 0$, a simple relation for DW velocity, v, is easily obtained from the model:

$$v = \frac{\Delta\gamma}{\alpha} H \,,$$ (4.1)

where the prefactor is known as the DW mobility, $\mu = \gamma\Delta/\alpha$. The transition between steady state DW motion and oscillatory DW motion $\dot{\psi} \neq 0$ happens when the applied field exceeds the Walker breakdown field given by:

$$H_{WB} = \frac{1}{2}\alpha H_K.$$ (4.2)

The maximum DW velocity at $H = H_{WB}$ follows directly from these equations:

$$v_{Max} = \frac{1}{2}\gamma\Delta H_K \,.$$ (4.3)

4.4.1 Measured DW Velocity Profile in 1D Model Framework

We will now compare the measured DW velocity profiles, $v(H)$, as shown in Figure 4.2 (b) with the 1D model expectations. In order to correctly account for the changes in various magnetic material properties some extra care needs to be taken. First the anisotropy field, H_K, as used in the 1D model is an effective anisotropy. The effective anisotropy also accounts for the energy gain that is obtained by the DW by taking advantage of the full 3D size of the nanowire: the DW forms a vortex structure rather than a transverse structure. However, effective or not, the anisotropy field in permalloy nanowires purely originates from shape-anisotropy only. Shape anisotropy on its turn is dependent on the saturation magnetization M_S, which varies over the osmium doped sample range. As noted above, the effective anisotropy can also be affected by changes in the DW structure. When it is assumed that no DW structure changes occur over the sample series, an assumption that will be supported by measurements of the DW width

later on, we obtain a linear dependence of the anisotropy field on the saturation magnetization: $H_K \propto M_S$.

The width, Δ, of DWs is determined by a competition between minimization of exchange energy A (by aligning individual spins) and minimization of anisotropy energy (by aligning individual spins with the nanowire). From Neél wall calculations one obtains the following expression for the DW width:

$$\Delta \propto \sqrt{\frac{A}{H_K}} \; . \tag{4.4}$$

Even though the DWs in our experiments will have the vortex structure it is still expected to have the linear dependence given by equation (4.4) as the structure is still determined by a competition between the same two energy terms.

As noted above the exchange energy is expected to decrease linearly with T_C and H_K decreases linearly with M_S. The relative decrease in T_C and M_S is of comparable magnitude, see Figure 4.1 (b and c), and thus the DW width, Δ, does not change with osmium doping, in first order approximation.

Now that we have obtained the proper material parameters and their dependency on osmium doping we can continue with the more phenomenological comparison of the key characteristics of the DW velocity profile, $v(H)$.

The maximum DW velocity of $v = 191$ m/s, reached in the lower osmium concentration samples for a field of about 8 to 9 Oe is two times bigger than DW velocities reported before by Beach et al. [63] in permalloy nanowires (with no osmium doping) with a cross-section of 20×600 nm. Which is in perfect agreement with the expectations from equation (4.3) if a growth of DW width linear with the nanowire width is assumed, as also predicted by micro-magnetic simulations by Nakatani et al. [22].

Plotting the inverse DW mobility, μ^{-1}, as obtained from a linear fit to the data points below H_{WB} in Figure 4.2 (b), against the Gilbert damping alpha, reveals a linear dependence, see Figure 4.3 (a). The slope in this figure is a direct measure for the DW width through equation (4.1) and results in a DW width of $\Delta = 13$ nm . The linearity of Figure 4.3 (a) is another indication that the DW indeed does not change its structure.

Another measure for the DW width would be the ratio of the Walker breakdown field and the maximum velocity at the Walker breakdown field, in which case the anisotropy field H_K is divided out, see equations (4.2) and (4.3) . In Figure 4.3 (b) this ratio is plotted again against the Gilbert damping alpha, and from the slope we again determine the DW width, which is now $\Delta = 14$ nm.

The so obtained DW widths are not only consistent in itself they are also in good agreement with measurements reported by Beach et al. [63]. However, these results are slightly smaller than expected from micro-magnetic simulations [22] (about 25% smaller).
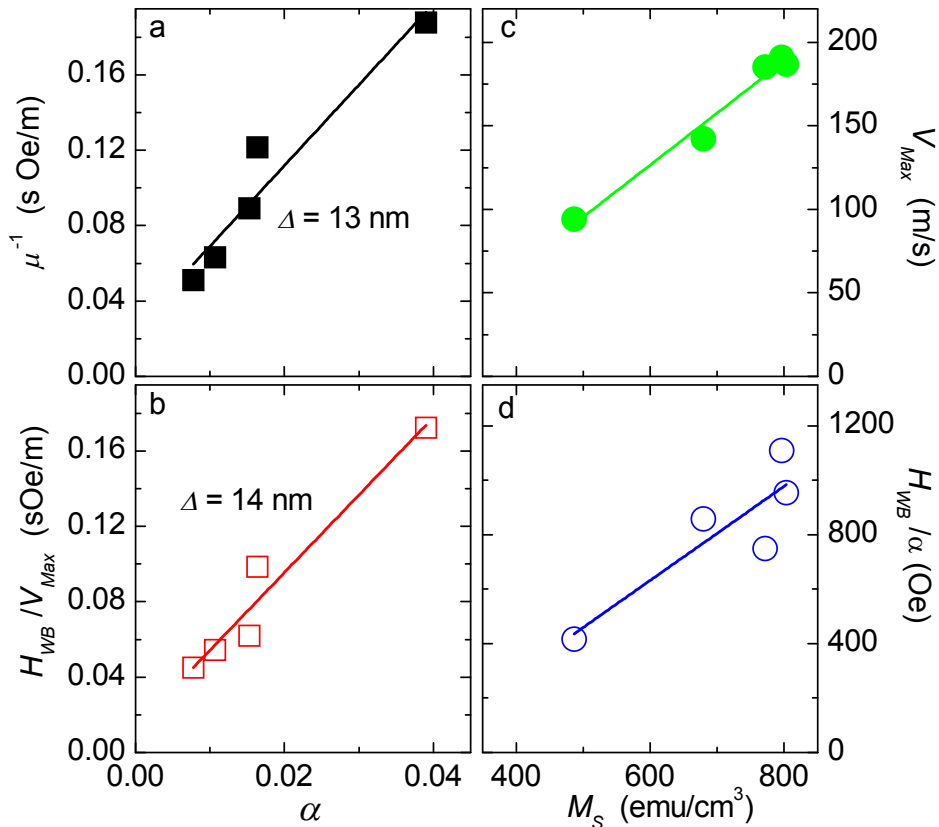

Figure 4.3 Dependence of (a) inverse DW mobility, μ^{-1}, and, (b) ratio of Walker breakdown field H_{WB} to maximum DW velocity v_{max} on Gilbert damping α. Dependence of (c) v_{max} and (d) H_{WB}/α on saturation magnetization M_S.

By plotting the maximum velocity, v_{max}, against the magnetization, M_S in Figure 4.3 (c) again a linear dependence is obtained. Through equation (4.3) we conclude that indeed H_K depends linearly on the magnetization M_S.

Finally another ratio of interest could be plotted, the ratio of the Walker breakdown field H_{WB} and the Gilbert damping α itself, see Figure 4.3 (d). Through equation (4.2)

we conclude that this is a direct measure of the effective anisotropy field, $H_K/2$. Indeed H_K increases linearly with increasing M_S.

4.4.2 Dynamic Propagation Field

Besides the DW dynamics itself also the minimum field needed to keep dynamic DWs propagating has a dependence on the level of osmium doping, the higher doped samples needed higher fields to keep DWs propagating. Figure 4.4 (c) shows a measurement of the dynamic propagation field H_P^D versus the Gilbert damping α. Clearly the dynamic propagation field increases first quickly with increasing Gilbert damping to eventually saturate to a certain maximum field.

To explain this dependence we follow the approach proposed in chapter 2.4 to simulate the wire roughness in the 1D model with a simple sinus with a wavelength of 500 nm. Note that we argued in chapter 2.4 that the Fourier component of interest for wire roughness should be around the same size as the DW width. This DW width refers to the real, or physical DW width[i]. The effective DW width as used in the 1D model equations, Δ, is significantly smaller (~14 nm) which is explained with the core of the vortex DW that dominates the DW dynamics [22]. The potential energy is than given by the sum of this sine-roughness and the Zeeman energy from the applied field:

$$E_P = 2M_S H S x + V \cos(2\pi \frac{x}{\lambda}),\qquad(4.5)$$

where S is the cross-section of the nanowire, V the amplitude of the roughness and λ the wavelength. The black line in Figure 4.4 (a) is an example of such an energy potential when a field of 10 Oe is applied and a roughness V is assumed such that the static propagation field, H_P^S, would be 15 Oe. Note that the static propagation field is just that field needed to overcome the potential barrier formed by the roughness:

$$H_P^S = \frac{\pi V}{\lambda M_S S}.\qquad(4.6)$$

---

[i] Still the definition of this *physical* DW width is ambiguous as the magnetization varies continuously from one orientation to the other; when some sensible definition is chosen, e.g. the region where 90% of the rotation happens, a *physical* DW width in the order of the width of the nanowire will be found.
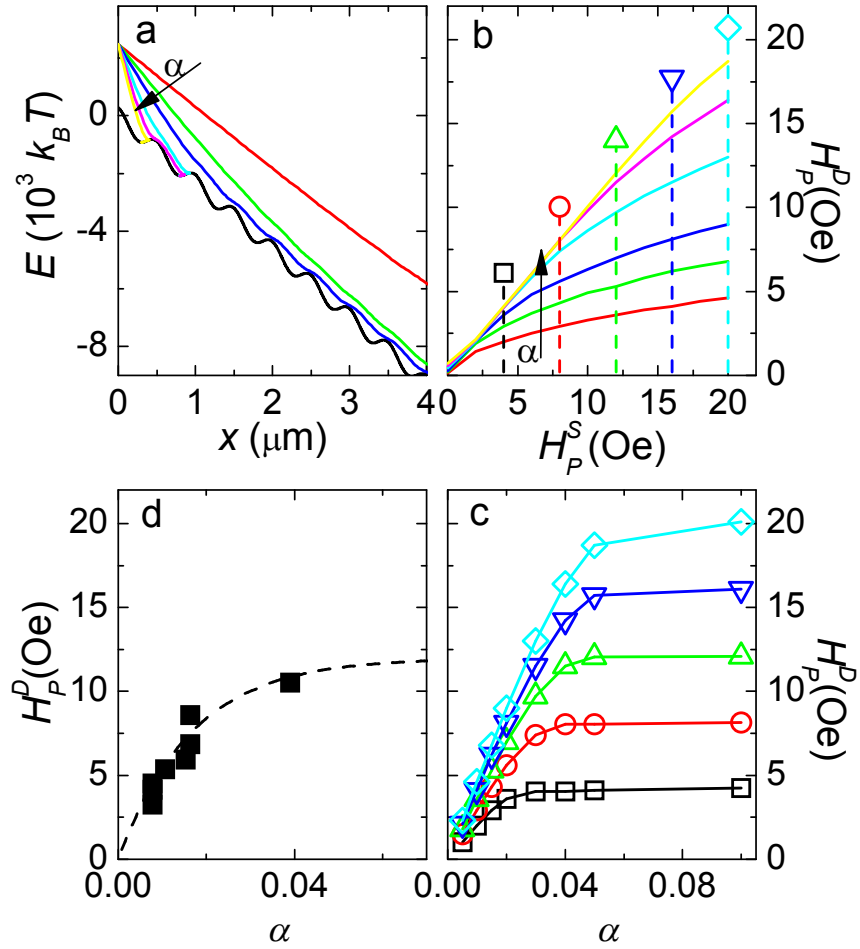
Figure 4.4 (a-c) 1D model calculation of DW motion in a permalloy nanowire (300 nm × 20 nm) with varying roughness and α. (a) DW energy landscape in a nanowire with roughness corresponding to $H_P^S = 15$ Oe, in an applied field $H = 10$ Oe for a DW at rest (black line) and for DWs with energy at $x = 0$ corresponding to $\psi = \pi/4$. The energy of the dynamic DWs is shown for α varying from 0.01 to 0.05 (increasing in the direction of the arrow). (b) Minimum field needed to sustain DW propagation H_P^D versus H_P^S for increasing Gilbert damping (for the same range of α as in a). (c) Cross-sections from calculation in (b) as marked by the dashed lines with matching symbols in (b). (d) Measured dynamic propagation field versus α. The dashed line is a guide to the eye.

1D model calculations are now performed for DWs injected at $x = 0$ with an initial out of the plane canting of the internal magnetization: $\psi > 0$ to simulate dynamic DWs.

Colored lines in Figure 4.4 (a) show the trajectories of these DWs for varied Gilbert damping coefficients α. Clearly the DWs with low damping are able to fly over the roughness energy barriers without being hold back. However, when damping increases there is a point where DWs are no longer able to fly over the energy roughness and get trapped in one of the local minima. Once trapped the field needed to start DW motion again is the static propagation field as given by equation (4.6). By varying the applied field and checking if a DW flies over or gets trapped in the roughness profile a minimum field at which such a DW propagates is determined. This field is called the dynamic propagation field H_P^D and is dependent on the roughness H_P^S and the Gilbert damping. Figure 4.4 (b) shows the dynamic propagation field versus the static propagation field for the same series of Gilbert damping coefficients α. For very high damping both propagations fields become equal. At such high damping the DW will propagate quasi statically and follow closely through the energy profile. At damping coefficients more closely to what is expected in permalloy and even in osmium doped permalloy, DWs are able to propagate at much lower applied fields than what one would expect from the roughness (H_P^S). To obtain a Gilbert damping dependence of the dynamic propagation field as measured in Figure 4.4 (c) we can take the data at cross-sections indicated by the dashed lines in Figure 4.4 (b), the result is shown in Figure 4.4 (d). With increasing Gilbert damping, the dynamic propagation field increases until it reaches the value of the static propagation field. At fields higher than the static propagation field no energy barriers are left and DWs will always propagate.

Side by side comparison of the measured dynamic propagation field, Figure 4.4 (c), and the dynamic propagation field form the 1D model calculation, Figure 4.4 (d), reveals remarkable equivalence. The 1D model shows saturation of the dynamic propagation field to the static propagation field when the Gilbert damping increases. From the propagation field measurements of static DWs in chapter 3 we know that the static propagation field in our nanowires is about 12-15 Oe. Indeed in the measurement here of the dynamic propagation field we observe saturation at a field of around 12 Oe.

4.5 Conclusion

We conclude that the simple sinusoidal model for wire roughness is robust enough to also describe systems with varied Gilbert damping predicting the dynamic propagation field in a quantitative way. Large increase of Gilbert damping has been achieved by doping permalloy films with up to 6% osmium. Measurement of DW velocity and the Walker breakdown field in samples with increasing osmium doping showed good agreement with the 1D model for DW motion when also the suppression of M_S and A are taken into account. Furthermore, our work demonstrates that Gilbert damping cannot only be used as a parameter to change the field dependent DW velocity, but also it has a dramatic effect on the minimum field needed to sustain DW motion. The resulting damping dependence of this dynamic propagation field can be well accounted for by the 1D model when including a simple model for wire roughness.

Current Assisted Domain Wall Motion

Ratio of adiabatic and non-adiabatic spin momentum transfer in permalloy nanowires as a function of osmium doping[i]

Domain wall velocity profiles as function of applied field and current are measured in osmium doped permalloy nanowires. Current through the nanowires is applied to aid or oppose the field driven domain wall motion through the spin momentum transfer effect. Walker breakdown field and maximum domain wall velocity are shown to be affected by the applied current. From comparison to simple 1-dimensional model expressions, numerical values are obtained for the electron spin polarization P and the non-adiabatic spin momentum transfer contribution β. Repeating these measurement in an osmium doped permalloy sample series reveals the spin torque efficiency dependence on osmium doping.

---

[i] Parts of this chapter are prepared for submission to Physical Review Letters

5.1 Introduction

Propagation of magnetic domain walls (DWs) in nano-sized magnetic wires is elemental for the feasibility of several recently proposed memory and logic devices [8, 64-66]. This has stimulated considerable research into the field of current driven magnetization dynamics of domain walls in various nanowire devices [16, 60, 67]. However a thorough understanding of the spin transfer torque (SMT) mechanism remains to be developed and the central question is the origin and magnitude of the non-adiabatic contribution to STT, parameterized by β in the Landau-Lifshitz-Gilbert equation (LLG). Berger first introduced the non-adiabatic term as a consequence of the Stern-Gerlach force on conduction electrons by the gradient in the s-d exchange field [38]. Others argue this may arise from linear momentum transfer [34] or spin flip scattering [39]. The non-adiabatic contribution has been measured before by comparing de-pinning current thresholds with micro magnetic simulations [89] and by measuring the DW velocity through the Anisotropic Magneto Resistance (AMR) effect [60]. However the results are ambiguous because the measurement is done in an indirect way or because the signal to noise ratio is so low that it is hard to determine β with enough accuracy. We here present the separate measurement of β and the electron spin polarization P in osmium doped permalloy nanowires. Furthermore we investigate the link between βP and the Gilbert damping α, when Gilbert damping is increased by doping the permalloy films with osmium. This osmium doping likely also impairs the spin polarization P and thus separation of P and β would be imperative.

5.2 Experimental

We measured the field driven and current assisted velocity profile of a DW in a permalloy ($Ni_{80}Fe_{20}$) nanowire with a 0.4% osmium doping. From comparison of the obtained measurements to the 1-dimensional (1D) model for DW dynamics we deduct a value for the parameter β as well as the spin polarization P. Secondly the dependence of the non-adiabatic contribution to the DW velocity on osmium doping level is measured and shown to decrease with osmium doping. This decrease can, equivalent to the measurements on the 0.4% doped permalloy sample, be related to a decrease in β and/or P. However, measurement of the full velocity versus field profile, $v(H)$, versus applied current, J, has not been done on these samples and therefore the dependence of P on osmium doping can not be separated from β. P is expected to decrease with the

increasing number of scattering sites formed by the osmium atoms. Furthermore, over the range of osmium samples measured (0%-6%) the AMR effect is measured and reduced significantly, see Figure 5.1. A link between AMR effect and spin polarization could be intuitively anticipated [90]. Although such a relation is non-trivial, the pronounced reduction of AMR as function of Os concentration is an indication that a reduction of P could be expected.
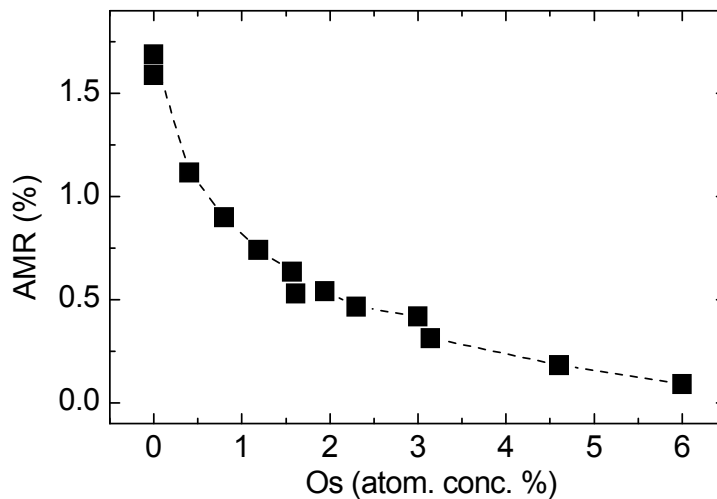

Figure 5.1 AMR effect as percentage of the total resistance of plain, 22 nm thick, permalloy films doped with increasing levels of osmium.

permalloy films of 22 nm thickness doped with osmium ranging in concentration from 0.0% to 6.0% are prepared by magnetron sputtering deposition, see chapter 4.3 for details on the preparation as well as for the magnetic properties of the so obtained NiFeOs material. 300 nm wide nanowires are formed by electron beam exposure and successive oxygen reactive ion etching on specially prefabricated CMOS chiplets containing buried Cu wires for local field pulse generation, see chapter 2.2.

We will now first determine β and P in a 0.4% osmium doped permalloy nanowire by measuring the DW velocity as function of applied field and current using the pump-probe magneto-optical Kerr effect microscopy technique as described in chapter 2. Successive comparison of the results with the 1D model expectations then results numerical values for the key parameters describing DW motion.

Pump-probe Kerr measurements where performed to determine the DW passage time at several positions along the 15 μm long nanowire. DW velocity is then determined by a linear fit to the data points. By varying the applied driving field H and repeating the

same velocity measurement a full DW velocity profile is obtained. By then varying the current that is applied with the field and either aids (negative J) or opposes (positive J) DW motion, the field dependent effect of current is obtained.

Figure 5.2 (a) shows the resultant DW velocity profile for five applied current densities J including zero current. Clearly the applied current causes the Walker breakdown field to shift to lower (higher) fields when the current applied aids (opposes) DW motion. Also the maximum DW velocity increases (decreases) when the current is aiding (opposing) the DW propagation. The DW mobility, dv/dH, below Walker breakdown remains constant under application of current. These observations are all directly expected from the 1D model, Equation (1.33) to (1.35).
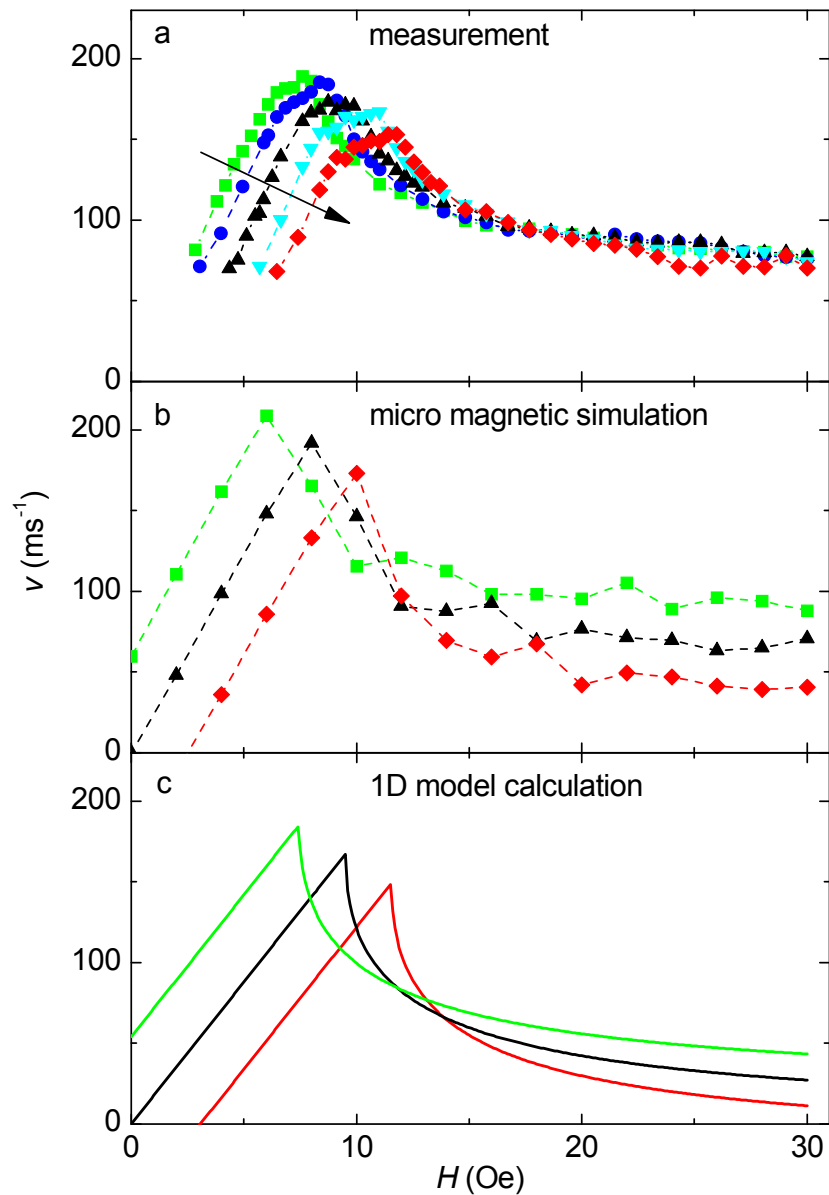
Figure 5.2 (a) DW velocity versus applied field when a current J of strength $(-0.50, -0.25, 0, 0.25, 0.50) \times 10^{12}$ A/m^2, increasing in direction of the arrow, is passed through the nanowire. Positive current is defined in the direction of the DW propagation. (b) Micro-magnetic simulation of DW velocity in 300×20 nm permalloy wire. Constants: $M_S = 800$ emu cm^{-3}, $\alpha = 0.01$, $\beta = 3\alpha$, $P = 0.5$, micro-magnetic cell size: $4 \times 5 \times 10$ nm, time-step: $\Delta t = 0.25$ ps. (c) 1D analytical model calculation using the same assumptions as in (b), in addition: $\Delta = 15$ nm and $H_K = 1900$ Oe.

5.3 One Dimensional Model Analysis

Figure 5.2 (b and c) show the DW velocities obtained from micro-magnetic simulation and from the analytical 1D model expressions. Micro-magnetic simulations [91] are performed on 300 × 20 nm permalloy nanowires of 1μm length. Moving boundary conditions are used to keep the propagating vortex DW structure in the middle of the nanowire. The average DW velocity is calculated by averaging over 40 ns of simulated DW propagation. Comparison of the data with the simulation and the 1D model analytical results show great similarity. In all cases the DW mobility is constant up to the Walker breakdown field and independent on the applied current. The Walker breakdown field shifts when current is applied and the above Walker breakdown DW velocities show little dependence on applied current.

Comparison of the DW mobility with the 1D model equations directly gives the value of the domain wall width: Δ = 14.9 nm given the Gilbert damping (α = 0.0092) as measured with FMR (see Figure 4.1), which is in agreement with theoretical expectations [22].

5.4 Analysis and Discussion

In Figure 5.3 the peak velocities and Walker breakdown fields are plotted as a function of the applied current density, J. The slope of the linear fit to the maximum velocity data directly reveals the spin polarization P from equation (1.35) and (1.31) in conjunction with the measured value for M_S = 799 emu/cm^3 . Thus we obtain P = 0.50. This is in accordance with estimates for the polarization in the literature which ranges from 0.4 to 0.7 [37].
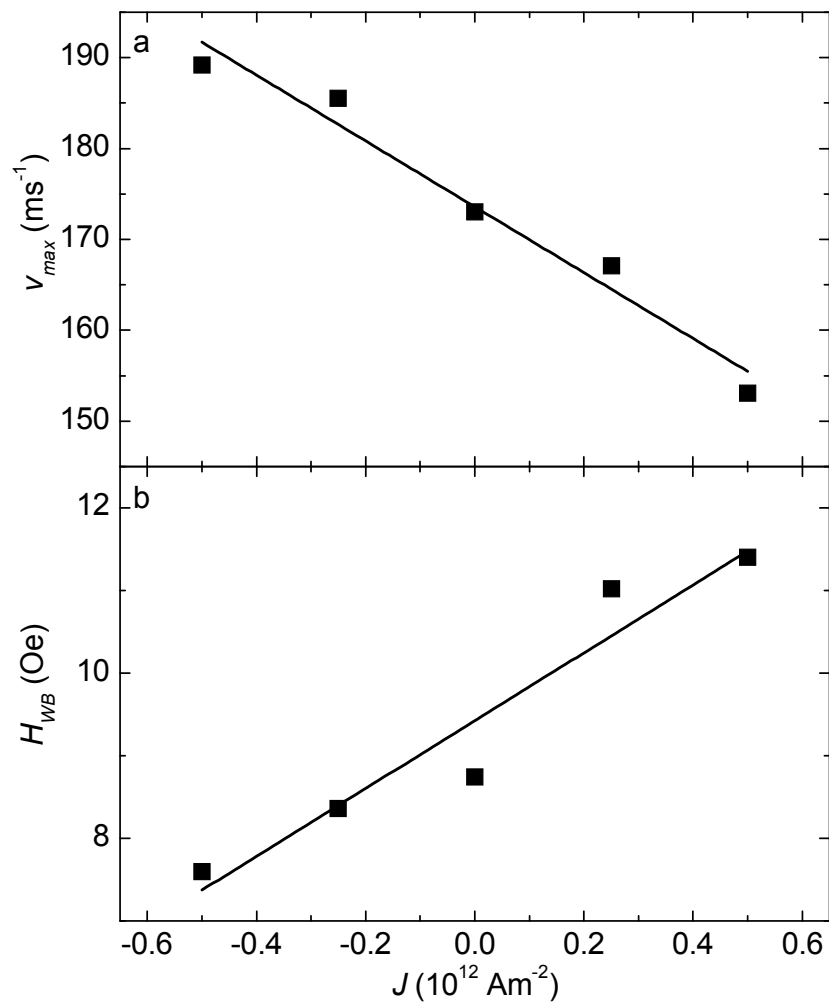
Figure 5.3 (a) Maximum DW velocity at Walker Breakdown field versus applied current density and linear fit to the data. (b) Walker breakdown field versus applied current density and linear fit to the data.

The maximum velocity at zero current together with the above calculated DW width, Δ, results in the effective anisotropy field, H_K = 1318 Oe. Included in this *effective* anisotropy field are shape anisotropy field as well as a reduction of that field due to the vortex rather than Bloch structure of the DW. The linear dependence of the Walker breakdown field as shown in Figure 5.3 (b) together with the above determined value for Δ and P as well the known value of α, results through equation (1.34) to the non-adiabatic parameter $\beta = 3.35\alpha$. Additionally, from the Walker breakdown field in absence of an applied current and the known value for α, the anisotropy field, H_K, can again be determined: H_K = 2037 Oe. The spread between the two differently obtained values for H_K is probably caused by the uncertainty in the determination of the peak value of the DW velocity. Another problem is that the cause for the breakdown in DW

velocity is the instability of the internal structure of the DW when Zeeman energy cannot be dissipated at a high enough rate to further enhance the DW velocity. It is likely that in a real nanowire the onset of the Walker breakdown is more complicated and for example affected by wire roughness. That the Walker breakdown is, in fact, more complicated can already be seen in the data of Figure 5.2. The DW velocity does not linearly increase up to H_{WB} but instead slows down already several Oersted before the field is reached.

A more direct measurement of β can be done when looking at the linear regime of DW propagation only. Figure 5.4 shows the change in DW velocity when current is applied with a driving field. The driving field here is chosen such that the sum of the driving field and applied current will not drive the DW velocity beyond the Walker breakdown field. From the slope of the data for the 0.4% osmium doped nanowire and the measured values for α, M_S and P, we deduce $\beta = 3.94\ \alpha$, in reasonable agreement with the estimate $\beta = 3.35\ \alpha$ obtained by applying equation (1.33). Note that there is still a value for the spin polarization P needed, which could only be deduced from the current induced change in peak DW velocity.

No full DW velocity profile measurements as function of current density have been successfully done on the other samples in the series with increasing osmium concentration. For these samples we will need to resort to other sources to determine P.
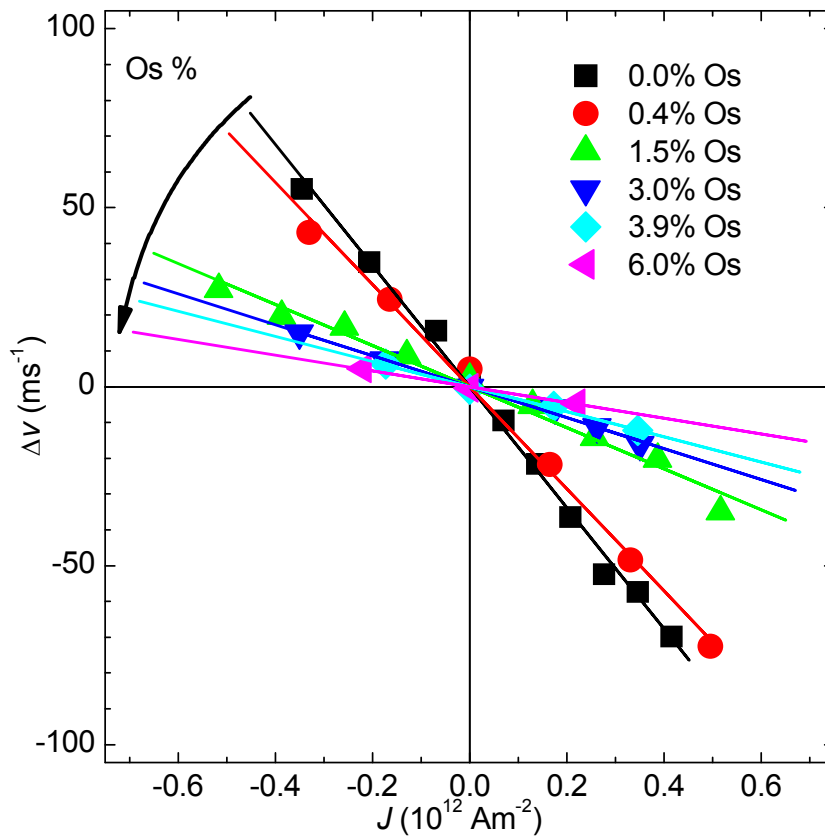
Figure 5.4 Velocity change due to current through the wire at a field below Walker breakdown for 300nm wide wires with increasing concentration of osmium doping. Driving field is fixed for each sample such that DW motion is limited to the linear regime. H = 5.6, 7.6, 8.0, 9.0, 9.0, 13.1 for the samples with increasing osmium doping respectively.

Equivalent to the description above for the 0.4% osmium doped sample, the non-adiabaticity parameter β can be determined for all samples in the series. Figure 5.4 shows the SMT induced change in DW velocity versus applied current for the whole series of osmium doped permalloy samples. These data were measured at an applied field strength such that DW motion remains in the linear regime. Clearly DW motion is affected more strongly when less osmium atoms are present and DW propagation stays in the linear regime within the current range applied as witnessed by the linear dependencies. From the consecutive slopes again βP can be determined. Since the maximum velocity could not be obtained no separate value for P is available.

If we assume that the polarization is not affected by the osmium atoms, and thus P remains $P = 0.5$ throughout the sample series we can plot β versus the Gilbert damping α, as shown in Figure 5.5.

The spin polarization P, however, is expected to drop with the increase of scattering sites formed by the osmium atoms as also argued from the measured AMR effect above. One possible approximation for the spin polarization is that it reduces at the same rate as the magnetization with the osmium doping. Figure 5.6 shows the non-adiabaticity constant β when this approximation for P is assumed. In both cases a significant drop in the non-adiabatic spin torque is observed when the Gilbert damping increases first, when further increase of the Gilbert damping is obtained not much further decrease of β is observed.
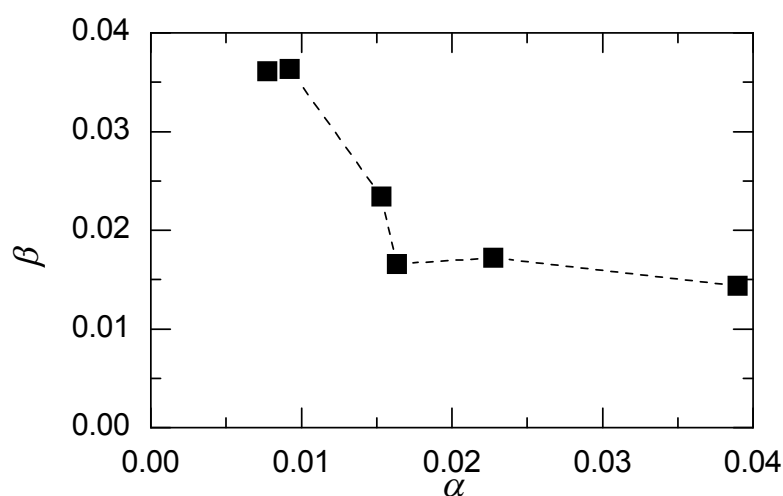

Figure 5.5 The spin torque efficiency, β as determined from $v(J)$ and the known values of α and M_S and by assuming $P = 0.5$ constant independent on osmium doping concentration.
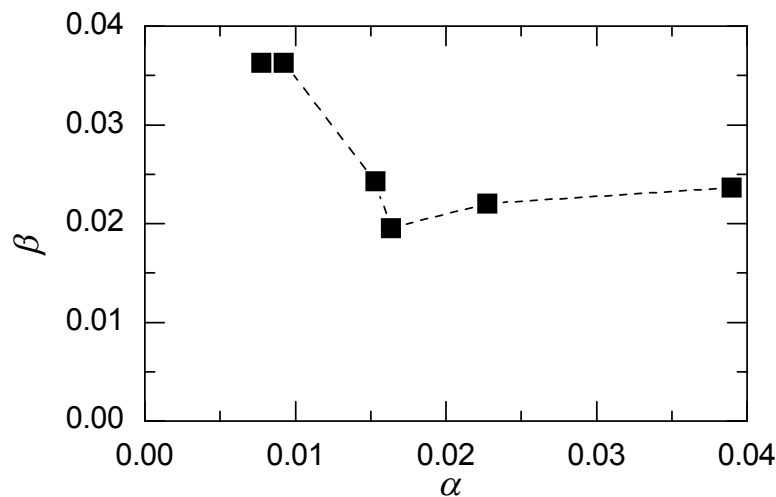
Figure 5.6 The spin torque efficiency, β as determined from $v(J)$ and the known values of α and M_S and by using the estimate $P = 0.5$ for osmium concentration of 0.4% and further assuming that P reduces proportional with M_S.

5.5 Conclusion

In conclusion we measured the non-adiabatic contribution to the SMT, parameterized by β and the electron spin polarization P in a permalloy nanowire with 0.4% osmium doping. Secondly we measured the dependence of the spin torque efficiency on osmium doping. A pronounced dependence of the measured non-adiabatic spin torque efficiency (βP) on Os concentration was found. This result may be interpreted as a sign that the intensively debated ratio β / α is far from constant over the range of alpha studied. However, for reaching an unambiguous conclusion more accurate and independent measurements of the spin polarization P are a necessity. Thus, achieving deeper insight on the link between β and α remains a challenge.

BIBLIOGRAPHY

1.   Wolf, S.A., et al., *Spintronics: A spin-based electronics vision for the future.* Science, 2001. **294**(5546): p. 1488-1495.

2.   Thomson, W., *On the Electro-Dynamic Qualities of Metals:--Effects of Magnetization on the Electric Conductivity of Nickel and of Iron.* Proceedings of the Royal Society of London, 1856-1857. **Vol. 8**: p. pp. 546-550

3.   Baibich, M.N., et al., *Giant Magnetoresistance of (001)Fe/(001) Cr Magnetic Superlattices.* Phys. Rev. Lett., 1988. **61**(21): p. 2472-2475.

4.   Binasch, G., et al., *Enhanced magnetoresistance in layered magnetic structures with antiferromagnetic interlayer exchange.* Physical Review B, 1989. **39**(7): p. 4828.

5.   Parkin, S.S.P., et al., *Giant tunnelling magnetoresistance at room temperature with MgO (100) tunnel barriers.* Nature Mater., 2004. **3**(12): p. 862-867.

6.   Akerman, J., *APPLIED PHYSICS: Toward a Universal Memory.* Science, 2005. **308**(5721): p. 508-510.

7.   Parkin, S.S.P., et al., *Exchange-biased magnetic tunnel junctions and application to nonvolatile magnetic random access memory (invited).* J. Appl. Phys., 1999. **85**(8): p. 5828-5833.

8.   Parkin, S.S.P., M. Hayashi, and L. Thomas, *Magnetic Domain-Wall Racetrack Memory.* Science, 2008. **320**(5873): p. 190-194.

9.   S.S.P.Parkin, *Shiftable magnetic shift register and method of using the same*, in *US Patent*. 2004: USA.

10.   Parkin, S.S.P., *System and method for writing to a magnetic shift register*, in *US Patent* 2004: USA.

11.   Parkin, S.S.P., *System and method for reading data stored on a magnetic shift register*. 2003 USA.

12.   Parkin, S.P.P., *Magnetic shift register with shiftable magnetic domains between two regions, and method of using the same*. 2004 USA.

13.   Parkin, S.P.P., *System and method for transferring data to and from a magnetic shift register with a shiftable data column* 2004 USA.

14. Thomas, L. and S. Parkin, *Current Induced Domain-wall motion in Magnetic nanowires*, in *Handbook of magnetism and advanced magnetic meterials*. 2007, John Wiley & Sons. p. 942-982.

15. Thomas, L., et al., *Resonant amplification of magnetic domain-wall motion by a train of current pulses.* Science, 2007. **315**(5818): p. 1553-1556.

16. Thomas, L., et al., *Oscillatory dependence of current-driven magnetic domain wall motion on current pulse length.* Nature, 2006. **443**(7108): p. 197-200.

17. Weiss, P., J. Physique Radium, 1907. **6**: p. 661.

18. Barkhausen, H., *Zwei mit Hilfe der neuen Verstarker entdeckte Erscheinungen.* Phys. Z., 1919. **20**: p. 401.

19. Bitter, F., *On the Magnetic Properties of Metals.* Physical Review, 1930. **36**(5): p. 978.

20. Martin, J.I., *Ordered magnetic nanostructures: fabrication and properties*

21. McMichael, R.D. and M.J. Donahue, *Head to head domain wall structures in thin magnetic strips.* IEEE Transactions on Magnetics, 1997. **33**(5 pt 2): p. 4167-4169.

22. Nakatani, Y., A. Thiaville, and J. Miltat, *Head-to-head domain walls in soft nano-strips: a refined phase diagram.* J. Magn. Magn. Mater., 2005. **290**: p. 750-753.

23. Miltat, J., G. Albuquerque, and A. Thiaville, *An Introduction to Micromagnetics in the Dynamic Regime*, in *Spin Dynamics in Confined Magnetic Structures I*. 2002. p. 1-33.

24. Thiaville, A. and Y. Nakatani, *Domain wall dynamics in nanowires and nanostrips*, in *Spin dynamics in confined magnetic structures III*. 2006, Springer Berlin / Heidelberg: Berlin. p. 1-50.

25. Gilbert, T.L., *A phenomenological theory of damping in ferromagnetic materials.* IEEE Transactions on Magnetics, 2004. **40**(6): p. 3443-3449.

26. Gilbert, T.L., *Formulation, Foundations and Applications of the Phenomenological Theory of Ferromagnetism.*, in *Illinois Institute of Technology*. 1956, Illinois Institute of Technology. p. 0037.

27. Gilbert, T.L. and J.M. JM Kelly, *Anomalous rotational damping in ferromagnetic sheets.* Conference proceedings of the 1st Magnetism and Magnetic Materials Conference, Pittsburgh, PA, June 14-16 1955, 1955.

28.   Goldstein, H., C. Poole, and J. Safko, *Classical mechanics*. San Francisco : Addison Wesley c2002. c2002. **3rd ed.**

29.   Landau, L.D. and E.M. Liftshitz, *L.D. Landau, Collected papers*, in *phys. Z. Sowjet.*, D.t. Haar, Editor. 1935, Gordon and Breach, New York. p. 153-169.

30.   Malozemoff, A.P. and J.C. Slonczewski, *Magnetic Domain Walls in Bubble Material*. 1979, New York: Academic Press.

31.   Döring, W., *On the inertia of the walls between Weiss Domains*. Zeit. Naturforsch, 1948. **3a**: p. 373-379.

32.   Berger, L., *Low-Field Magnetoresistance and Domain Drag in Ferromagnets*. J. Appl. Phys., 1978. **49**(3): p. 2156-2161.

33.   Slonczewski, J.C., *Current-driven excitation of magnetic multilayers*. J. Magn. Magn. Mater., 1996. **159**(1-2): p. L1-L7.

34.   Tatara, G. and H. Kohno, *Theory of current-driven domain wall motion: Spin transfer versus momentum transfer*. Phys. Rev. Lett., 2004. **92**(8): p. 086601.

35.   Li, Z. and S. Zhang, *Domain-wall dynamics and spin-wave excitations with spin-transfer torques*. Phys. Rev. Lett., 2004. **92**(20): p. 207203.

36.   Thiaville, A., et al., *Micromagnetic understanding of current-driven domain wall motion in patterned nanowires*. Europhys. Lett., 2005. **69**(6): p. 990-996.

37.   Beach, G.S.D., *Current-induced domain wall motion*. Journal of magnetism and magnetic materials, 2008. **320**: p. 1272-1281.

38.   Berger, L., *Exchange Interaction between Ferromagnetic Domain-Wall and Electric-Current in Very Thin Metallic-Films*. J. Appl. Phys., 1984. **55**(6): p. 1954-1956.

39.   Zhang, S. and Z. Li, *Roles of nonequilibrium conduction electrons on the magnetization dynamics of ferromagnets*. Phys. Rev. Lett., 2004. **93**(12): p. 127204.

40.   Mott, N.F., *The Electrical Conductivity of Transition Metals*. Proc. Roy. Soc. London, 1936. **A153**: p. 699.

41.   Berger, L., *Exchange Interaction between Electric-Current and Magnetic Domain-Wall Containing Bloch Lines*. J. Appl. Phys., 1988. **63**(5): p. 1663-1669.

42.   Berger, L., *Possible Existence of a Josephson Effect in Ferromagnets.* Phys. Rev. B, 1986. **33**(3): p. 1572-1578.

43.   Freitas, P.P. and L. Berger, *Observation of S-D Exchange Force between Domain-Walls and Electric-Current in Very Thin Permalloy-Films.* J. Appl. Phys., 1985. **57**(4): p. 1266-1269.

44.   Hung, C.Y., L. Berger, and C.Y. Shih, *Observation of a Current-Induced Force on Bloch Lines in Ni-Fe Thin-Films.* J. Appl. Phys., 1990. **67**(9): p. 5941-5943.

45.   Hung, C.Y. and L. Berger, *Exchange Forces between Domain-Wall and Electric-Current in Permalloy-Films of Variable Thickness.* J. Appl. Phys., 1988. **63**(8): p. 4276-4278.

46.   Berger, L., *Emission of spin waves by a magnetic multilayer traversed by a current.* Phys. Rev. B, 1996. **54**(13): p. 9353-9358.

47.   Barnes, S.E. and S. Maekawa, *Current-spin coupling for ferromagnetic domain walls in fine wires.* Phys. Rev. Lett., 2005. **95**(10): p. 107204.

48.   Tatara, G., H. Kohno, and J. Shibata, *Microscopic approach to current-driven domain wall dynamics.* Physics Reports, 2008. **468**(6): p. 213-301.

49.   Salhi, E. and L. Berger, *Current-Induced Displacements of Bloch Walls in Ni-Fe Films of Thickness 120-740 Nm.* J. Appl. Phys., 1994. **76**(8): p. 4787-4792.

50.   Gan, L., et al., *Pulsed-Cuffent-Induced Domain Wall Propagation in permalloy patterns observed using magnetic force microscopy.* IEEE Transactions on Magnetics, 2000. **36**: p. 3047.

51.   Yamaguchi, A., et al., *Real-space observation of current-driven domain wall motion in submicron magnetic wires.* Phys. Rev. Lett., 2004. **92**(7): p. 077205.

52.   Florez, S.H., C. Krafft, and R.D. Gomez, *Spin-current-induced magnetization reversal in magnetic nanowires with constrictions.* J. Appl. Phys., 2005. **97**(10): p. 10C705.

53.   Klaui, M., et al., *Direct observation of domain-wall pinning at nanoscale constrictions.* Appl. Phys. Lett., 2005. **87**(10): p. 102509.

54.   Klaui, M., et al., *Direct observation of domain-wall configurations transformed by spin currents.* Phys. Rev. Lett., 2005. **95**(2): p. 026601.

55.   Vernier, N., et al., *Domain wall propagation in magnetic nanowires by spin-polarized current injection.* Europhys. Lett., 2004. **65**(4): p. 526-532.

56. Yamaguchi, A., et al., *Reduction of threshold current density for current-driven domain wall motion using shape control.* Jpn. J. Appl. Phys., 2006. **45**(5A): p. 3850-3853.

57. Laufenberg, M., et al., *Temperature dependence of the spin torque effect in current-induced domain wall motion.* Phys. Rev. Lett., 2006. **97**(4): p. 046602.

58. Hayashi, M., et al., *Influence of current on field-driven domain wall motion in permalloy nanowires from time resolved measurements of anisotropic magnetoresistance.* Phys. Rev. Lett., 2006. **96**(19): p. 197207.

59. Nakatani, Y., A. Thiaville, and J. Miltat, *Faster magnetic walls in rough wires.* Nature Mater., 2003. **2**(8): p. 521-523.

60. Hayashi, M., et al., *Current driven domain wall velocities exceeding the spin angular momentum transfer rate in permalloy nanowires.* Phys. Rev. Lett., 2007. **98**(3): p. 037204.

61. Yamanouchi, M., et al., *Velocity of domain-wall motion induced by electrical current in the ferromagnetic semiconductor (Ga,Mn)As.* Phys. Rev. Lett., 2006. **96**(9): p. 096601.

62. Jubert, P.O., et al., *Velocity of vortex walls moved by current.* J. Appl. Phys., 2006. **99**(8): p. 08G523.

63. Beach, G.S.D., et al., *Dynamics of field-driven domain-wall propagation in ferromagnetic nanowires.* Nature Mater., 2005. **4**(10): p. 741-744.

64. Hayashi, M., et al., *Current-Controlled Magnetic Domain-Wall Nanowire Shift Register.* Science, 2008. **320**(5873): p. 209-211.

65. Allwood, D.A., et al., *Magnetic domain-wall logic.* Science, 2005. **309**(5741): p. 1688-1692.

66. Kostylev, M.P., Serga, A. A., Schneider, T., Leven, B., and Hillebrands, B., *Spin-wave logical gates.* Applied Physics letters, 2005. **87**(153501).

67. Tatara, G., H. Kohno, and J. Shibata, *Microscopic approach to current-driven domain wall dynamics.* Physics Reports-Review Section of Physics Letters, 2008. **468**(6): p. 213-301.

68. Thomas, L., et al., *Observation of injection and pinning of domain walls in magnetic nanowires using photoemission electron microscopy.* Appl. Phys. Lett., 2005. **87**(26): p. 262501.

69. Hayashi, M., et al., *Direct observation of the coherent precession of magnetic domain walls propagating along permalloy nanowires.* Nature Phys., 2007. **3**: p. 21.

70.   Meier, G., et al., *Direct Imaging of Stochastic Domain-Wall Motion Driven by Nanosecond Current Pulses.* Phys. Rev. Lett., 2007. **98**(18): p. 187202-4.

71.   Stoll, H., et al., *High-resolution imaging of fast magnetization dynamics in magnetic nanostructures.* Applied Physics Letters, 2004. **84**(17): p. 3328.

72.   Beach, G.S.D., et al., *Dynamics of field-driven domain-wall propagation in ferromagnetic nanowires.* Nat. Mater., 2005. **4**: p. 741-744.

73.   Cowburn, R.P., et al., *Domain wall injection and propagation in planar Permalloy nanowires.* J. Appl. Phys., 2002. **91**(10): p. 6949-6951.

74.   Cormier, M., et al., *High resolution polar Kerr magnetometer for nanomagnetism and nanospintronics.* Review of Scientific Instruments, 2008. **79**(3): p. 033706.

75.   Yang, S.Q. and J.L. Erskine, *Spin-transfer-torque-driven domin-wall dynamics in Permalloy nanowires.* Phys. Rev. B, 2007. **75**(22): p. 220403.

76.   Freeman, M.R. and B.C. Choi, *Advances in Magnetic Microscopy.* Science, 2001. **294**: p. 1484-1488.

77.   Rosenberg, R., et al., *Copper metallization for high performance silicon technology.* Ann. Rev. Mater. Sci., 2000. **30**: p. 229-262.

78.   Jozsa, C., et al., *Retrieving pulse profiles from pump-probe measurements on magnetization dynamics.* Journal of Applied Physics, 2004. **95**(11): p. 7447.

79.   Hayashi, M., et al., *Dependence of current and field driven depinning of domain walls on their structure and chirality in permalloy nanowires.* Phys. Rev. Lett., 2006. **97**: p. 207205.

80.   Jiang, X., et al., submitted, 2009.

81.   Tanigawa, H., et al., *Dynamical pinning of a Domain Wall in a Magnetic Nanowire Induced by Walker Breakdown.* PRL, 2008. **101**(207203): p. 207203.

82.   Ravelosona, D., et al., *Nanometer scale observation of high efficiency thermally assisted current-driven domain wall depinning.* Phys. Rev. Lett., 2005. **95**(11): p. 117203.

83.   Laribi, S., et al., *Reversible and irreversible current induced domain wall motion in CoFeB based spin valves stripes.* Appl. Phys. Lett., 2007. **90**(23): p. 232505.

84. Tanigawa, H., et al., *Current-Driven Domain Wall Motion in CoCrPt Wires with Perpendicular Magnetic Anisotropy.* Applied Physics Express, 2008. **1**(1): p. 011301.

85. Yamanouchi, M., et al., *Current-induced domain-wall switching in a ferromagnetic semiconductor structure.* Nature, 2004. **428**(6982): p. 539-542.

86. Tatara, G., et al., *Threshold current of domain wall motion under extrinsic pinning, beta-term and non-adiabaticity.* J. Phys. Soc. Jpn., 2006. **75**(6): p. 064708.

87. Parkin, *Increased damping of magnetization in magnetic materials*, in *US Patent*. 2002: USA.

88. Sangita, S.K., et al., *Ferromagnetic resonance linewidth in metallic thin films: Comparison of measurement methods.* Journal of Applied Physics, 2006. **99**(9): p. 093909.

89. Lepadatu, S., et al., *Dependence of Domain-Wall Depinning Threshold Current on Pinning Profile.* Physical Review Letters, 2009. **102**(12): p. 127203.

90. McGuire, T.R. and R.I. Potter, *Anisotropic Magnetoresistance in Ferromagnetic 3d Alloys.* IEEE Trans. Magn., 1975. **11**(4): p. 1018-1038.

91. Scheinfein, M.R., *LLG Micromagnetics Simulator^{TM}*.

ABSTRACT

Magnetization Dynamics in Racetrack Memory

Various devices have been proposed which use magnetic domain walls (DWs) in nano-sized magnetic structures to perform logic operations or store information. In particular in 'Racetrack memory' bits of information represented by DWs are shifted in a magnetic wire to be stored. For these memory and logic devices to be successful, great control of DW motion is of vital importance.

In cooperation with IBM's Almaden research laboratory a pump-probe Kerr magneto-optical scanning microscope has been developed. In order to control DW injection, motion and reset, magnetic fields have to be applied locally on the nanowire. For this a special Damascene CMOS chip has been fabricated at the 200 mm wafer facility at IBM Microelectronics Research Laboratory (MRL). Probing of the local magnetization is done with a focused pulsed laser spot of 400 nm diameter where the polarization rotation caused by the Kerr effect is measured after reflection. In order to achieve optimal focusing a perpendicular incident laser beam is focused with a high numerical aperture objective. Synchronized 'pumping' in this scheme is achieved by successively: 1 injecting a DW; 2 propagate the DW down the nanowire with either current through or an applied field pulse over the nanowire; 3 and finally resetting the whole nanowire to its original magnetization by applying a large field together with the injection of an opposite magnetic domain. With this setup field and current induced DW motion is studied in permalloy nanowires ranging in width from 200 to 700 nm and thickness of 20 nm.

For control of DWs in Racetrack memory it is important to understand the different mechanism for driving a DW already in motion (dynamic) and driving a DW that is currently at rest (static). The propagation field, the minimum field below which no DW motion takes place, is measured for both dynamic DWs and static DWs. It is found that Static DWs require a much higher field than DWs already in motion. A model is build where this effect is related to the wire roughness, successfully describing the existence of a propagation field, the difference between both propagation fields and a specific effect related to the method of injection.

For Racetrack memory to be successful the critical current needs to be small (the current needed to move a DW solely by current) and the DW velocity high. Much of the influence of intrinsic magnetic properties of materials on DW dynamics is unknown. One important property affecting DW velocity and possibly also the critical current is Gilbert damping. Gilbert damping in permalloy can be tuned by doping the nanowires with osmium. This is used to prepare a sample series with increasing Gilbert damping. Measurement of the field induced DW velocity revealed a profile well known that includes the Walker breakdown (a maximum field where further increasing field strength does not further increase the DW velocity). From this profile the dependence of the Walker breakdown, DW mobility and maximum DW velocity on Gilbert damping has been determined.

With the same sample series also current induced field assisted DW motion has been measured. Current induced DW motion is known to be driven by two effects: adiabatic- and ballistic- spin momentum transfer (SMT) which relative contribution is parameterized by beta in the Landau Lifshitz Gilbert equation (LLG). Measurement of DW velocity depending on current density revealed the relative contribution of the two SMT schemes. Also the influence of Gilbert damping on the relative contribution of both schemes has been explored. A pronounced dependence of the measured spin torque efficiency on osmium concentration was found. This result may be interpreted as a sign that the intensively debated ratio β / α is far from constant over the range of α studied.

SAMENVATTING

Magnetizatie Dynamica in Racetrack Geheugen

Er zijn in de literatuur diverse concepten voorgesteld voor het verwerken (logica) en het opslaan (geheugen) van informatie door middel van magnetische domeinen in een magnetisch materiaal. Over het algemeen spreekt men van domain grenzen (DGs), de grens tussen twee domeinen met verschillende magetizatie. Het is aangetoond dat dergelijke DGs in zekere zin kunnen worden opgevat als vrije deeltjes die zich in magnetische structuren van nano-afmetingen kunnen verplaatsen; bijvoorbeeld structuren van een magnetisch materiaal zoals die op een chip gemaakt zouden kunnen worden. Racetrack memory, zoals besproken in deze thesis, is een geheugen concept waarbij eenheden van informatie worden opgeslagen in de vorm van DGs in een magnetische nano-draad. Door deze DGs in de draad heen en weer te schuiven kunnen ze gelezen en geschreven worden. Voor dergelijke logica en geheugen concepten is perfecte controle van de dynamica van de magnetische DGs van het grootste belang.

In samenwerking met de onderzoeks afdeling van IBM in Almaden is er een stroboscopische magneto-optische Kerr meetmethode ontwikkeld. Om de formatie en propagatie van DGs te initiëren moet een sterk gelokaliseerd magnetisch veld worden aangelegd. Hiervoor is een speciale Damascene CMOS chip gemaakt in de 200 mm wafer fabriek van IBM, het Microelectronics Research Laboratory (MRL). Het meten van de lokale magnetizatie in de nanodraad wordt gedaan door een stroboscopisch pulserende laser te convergeren tot een punt op de nanodraad. Het Kerr effect zorgt ervoor dat de polarizatie van het licht verandert na reflectie van de magnetische nanodraad. Door de mate van polarizatie verandering te meten, kan de magnetizatie van de nanodraad ter plaatse worden vastgesteld. Door synchroon met de pulserende laser, doch met kleine, variabele, tijdsvertraging, DGs in de draad te injecteren en langs de draad te propageren kan de dynamica van DGs gemeten worden. Met deze meetmethode is veld en stroom geïnduceerde DG propagatie bestudeerd in nanodraden van NiFe met een breedte van 200 tot 700 nm en een dikte van 20 nm.

Voor de optimale controle van DG propagatie in Racetrack geheugen is het belangrijk om het verschil te begrijpen tussen DGs die al in beweging zijn (dynamische DGs) en

DGs die stil staan (statische DGs). Het minimum veld nodig om DG propagatie te bewerkstelligen is gemeten voor beide gevallen. Het blijkt dat statische DGs een veel hoger veld nodig hebben om in beweging te komen dan dynamische DGs nodig hebben om in beweging te blijven. Dit effect is gemodelleerd door het DG propagatie veld te relateren aan de ruwheid van de nanodraad. Dit model beschrijft succesvol het bestaan van een propagatie veld alsmede een verschil tussen het dynamische en statische propagatieveld zoals gemeten.

Om Racetrack geheugen tot een succes te maken is het nodig de kritische stroom, de minimum stroom nodig om DG propagatie zonder veld te bewerkstelligen, omlaag te brengen. Bovendien moet de DG propagatie snelheid hoog zijn, omdat de snelheid van het Racetrack geheugen daar direct van afhankelijk is. Er is nog niet veel bekend over de invloed van fundamentele materiaal eigenschappen op de hoogte van de kritische stroom en de snelheid van DG propagatie. Een belangrijke materiaal eigenschap die van invloed is op de DG propagatie snelheid en misschien ook invloed heeft op de kritische stroom, is de Gilbert demping. Gilbert demping in NiFe kan aangepast worden door de nanodraden te doteren met osmium. Door een serie gelijke NiFe nanodraden te doteren met een toenemende concentratie osmium is een serie met toenemende Gilbert demping verkregen. Metingen van de veld geïnduceerde DG snelheid leverde het bekende profiel op met de Walker ineenstorting (een maximum veld sterkte waarbij verdere verhoging van het veld geen verdere verhoging van de DG snelheid opleverd). Van dit profiel is de afhankelijkheid van de Walker ineenstorting, de DG mobiliteit en de maximum DG snelheid van Gilbert demping herleid.

Op dezelfde serie nanodraden zijn ook metingen gedaan van de stroom geïnduceerde, veld geassisteerde DG propagatie. Stroom geïnduceerde DG propagatie wordt veroorzaakt door twee fundamentele effecten: adiabatische- en ballistische- spin moment overdracht (SMO) waarbij hun relatieve bijdragen zijn geparameterizeerd met beta in de Landau Lifshitz Gilbert vergelijking (LLG). Metingen van de DG snelheid afhankelijk van stroomsterkte heeft een directe bepaling van deze parameter beta opgeleverd. Verder is ook de invloed van Gilbert demping op deze relatieve bijdrage aan de twee SMO mechanismen verkend. Een sterke afhankelijkheid van de gemeten spin koppel efficiëntie van osmium dotering is gevonden. Dit resultaat kan worden geïnterpreteerd als een teken, dat de in de literatuur uitgebreid bediscussieerde ratio van β / α zeer zeker niet constant is over de hier geëvalueerde reeks van Gilbert dempingen.

LIST OF PUBLICATIONS

Measurement of non-adiabaticity constant beta in permalloy nanowires and outlook at link between beta and Gilbert damping.

Bastiaan Bergman, Rai Moriya, Luc Thomas, Xin Jiang, See-Hun Yang, Masamitsu Hayashi, Bert Koopmans, Stuart S.P. Parkin

In Preparation

Field driven domain wall dynamics in magnetic nanowires when Gilbert damping is varied

Bastiaan Bergman, Rai Moriya, Masamitsu Hayashi, Luc Thomas, See-Hun Yang Bert Koopmans, Stuart S.P. Parkin

To be Submitted

An investigation of the static and dynamic domain wall propagation fields in permalloy nanowires using pump-probe Kerr microscopy

Bastiaan Bergman, Rai Moriya1, Masamitsu Hayashi, Luc Thomas, Bert Koopmans, Stuart S.P. Parkin

To be Submitted

Single-shot real-time measurements of stochastic magnetic field driven domain wall motion using a spin-valve nanowire

Xin Jiang, Rai Moriya, Masamitsu Hayashi, Luc Thomas, Bastiaan Bergman, Charles Rettner, and Stuart S. P. Parkin

To be Submitted

Generation of local magnetic fields at MHz rates for the study of domain wall propagation in magnetic nanowires

Bastiaan Bergman, Rai Moriya, Masamitsu Hayashi, Luc Thomas, Christy Tyberg, Yu Lu, Eric Joseph, Mary-Beth Rothwell, John Hummel, William J. Gallagher, Bert Koopmans, Stuart S.P. Parkin

Submitted to Applied Physics Letters

Identifying growth mechanisms for laser induced magnetization in FeRh

B. Bergman, G. Ju, J. Hohlfeld, R.J.M. van de Veerdonk, J.-Y. Kim, X. Wu, D. Weller and B. Koopmans

Phys. Rev. B 73 60407-1 (2006)

Ultrafast generation of ferromagnetic order via laser-induced phase transformation in FeRh thin films

G. Ju, J. Hohlfeld, B. Bergman, R.J.M. van de Veerdonk, O.N. Mryasov, J.-Y. Kim, X. Wu, D. Weller and B. Koopmans

Phys. Rev. Lett. 93, 197403 (2004)

CURRICULUM VITAE

Bastiaan Bergman, born on July 10th, 1973 in Schiedam, The Netherlands, obtained his mavo high school diploma in June 1990 in Groningen. After attending the laboratory school for applied chemistry in Groningen and Leiden he obtained his theory certificate from the Leiden school in June 1993 which gave access to the Eindhoven polytechnic of engineering in the department of applied physics. In Eindhoven he became a member of the Eindhovens Studenten Corps (ESC) and fraternity Alcibiades. He received his propaedeutic diploma in January 1995 and continued his study of applied physics at the Eindhoven University of Technology. During his time in Eindhoven Bastiaan was a member in various committees and boards organizing Eindhovens student life and led the student fraction of the department participation board. Besides his study Bastiaan acquired numerous side jobs, ranging form dishes at the *van Breukelen brasserie* to co-editor of a third year course on sustainable development which is still taught today at the TU/e.

Bastiaan earned his Masters of Science (MSc) degree in Applied Physics at the Eindhoven University of Technology in August 2004. His graduate research was performed at Seagate Technology, in Pittsburgh, Pennsylvania, USA. At Seagate he investigated spin precession in Heat Assisted Magnetic Recording (HAMR) media, the believed successor of today's Hard Disc Drive technology. Bastiaan and his colleagues at Seagate were the first to measure the ultrafast magnetic phase change of thin FeRh films when heated with femto second laser pulses. Parts of his thesis "Probing Spin Dynamics in Ultrafast Anti-Ferromagnetic to Ferromagnetic Phase Transitions" were published in Physical Review Letters and presented at international conferences.

In January 2005 Bastiaan started his current job at the IBM Almaden Research laboratory in San Jose, California, USA, where he performed the work presented in this thesis.

ACKNOWLEDGEMENT

Masamitsu Hayashi, See-Hun Yang, Xin Jiang of the IBM racetrack team. The people in IBM MRL: Christy Tyberg, Yu Lu, Eric Joseph, Mary-Beth Rothwell, John Hummel and William Gallagher, thank you for the design and production of the CMOS chips.

Than, in the last paragraph of my thesis, I want to thank my parents Kees and Marly, for their long breath in supporting me throughout my scholar career; my wife, Marguerite, for her optimism and positivism during all the ups and downs that are accompanied with 'doing' a Ph.D. program and, finally, I am thankful to my son Constantijn, just for being so wonderful!